Multiphase Modelling of Liquid Atomisation using VoF-LES in an Internal Mixing Twin-Fluid Swirl Nozzle

Mads Andreas Nielsen & Mathias Bennedsgaard Olesen

Thermal Energy and Process Engineering, TEPE4-1008 2024-5

Master's Thesis

Aalborg University
http://www.aau.dk

AALBORG UNIVERSITY

STUDENT REPORT

Title:
Multiphase Modelling of Liquid Atomisation using VoF-LES in an Internal Mixing Twin-Fluid Swirl Nozzle

Project Period:
Spring Semester 2024

Project Group:
TEPE4-1008

Participants:
Mads Andreas Nielsen
Mathias Bennedsgaard Olesen

Supervisor:
Jakob Hærvig

Company Supervisor:
Kasper Gram Bilde

Copies: 1

Page Numbers: 58

Date of Completion:
May 31, 2024

Abstract:

Twin-fluid nozzles are widely used for atomization applications such as fuel injection, spray painting, and gas cooling. In this study, an internal mixing twin-fluid swirl nozzle has been investigated numerically using CFD. Air and water were used as working fluids at low Reynolds numbers of 1980 to 5650. Large eddy simulations were carried out using the volume of fluid method. The simulated Sauter Mean Diameter (SMD) deviated 16.9 % from experimental data. The effect of varying the gas-to-liquid mass flow ratio (GLR) on the atomization performance revealed that a 20 % increase in GLR resulted in a 2.8 % decrease in the SMD. The spray symmetry was also investigated using the time-averaged water volume fractions. The analysis revealed asymmetrical spray patterns downstream of the nozzle. Geometrical changes were made to study the influence of the inclination angle of the inlet pipes on the droplet size distribution and spray symmetry. The simulations showed that the SMD decreased by 11.9 % at an inclination angle of 0 ° compared to the baseline case of 27.5 °. When the inclination angle increased to 55 ° the SMD increased by approximately 8.3 %. The spray symmetry was slightly improved at inclination angles of 0 ° and 55 ° compared to 27.5 °.

Preface

This master's thesis project is written in the period 1st of February to 31st of May 2024 at the Department of Energy Technology at Aalborg University.

Reading Instructions

Throughout the project, references are made to relevant literature using the Harvard method, where the source in the text is referenced with (Author Year). References are listed in the back of the report.

Figures, tables, and equations are numbered according to the chapter in which they are located, e.g. the first figure in Chapter 2 is named "Figure 2.1". A caption text is placed below figures and above tables.

The appendices can be found at the back of this project, and they are listed with letters starting from A. In the main project, references to the appendices are written as e.g. "Figure A.1". The appendices contain information relevant to different parts of the main project.

Acknowledgements

The authors would like to acknowledge Alfa Laval Aalborg for providing the opportunity to work on this project and gain valuable experience. Furthermore, a thank you is extended to our company supervisor Kasper Gram Bilde for his support and guidance.

We would also like to sincerely thank our fellow student Esben Martinsen for his invaluable help and assistance with CFD software and sparring in terms of the project.

Mads Andreas Nielsen

Mads Andreas Nielsen
<mani19@student.aau.dk>

mathias olesen

Mathias Bennedsgaard Olesen
<mbol19@student.aau.dk>

Executive Summary

This study presents a numerical investigation of an internal mixing twin-fluid swirl nozzle using computational fluid dynamics (CFD). The aim was to understand the atomization performance of the nozzle and its sensitivity to variations in the gas-to-liquid mass flow ratio (GLR) and inclination angle of the inlet pipes, β. The main areas of focus were the prediction of the Sauter mean diameter (SMD) and the assessment of spray symmetry. The CFD simulations were validated using experimental data from Ochowiak (2016). The results deviated approximately 16.9 % from the experimental values.

The effect of varying the GLR on the atomization performance was investigated and the results are presented in Figure 1a. A 20 % increase in GLR resulted in a 2.8 % decrease in SMD. This observation is consistent with the findings in the literature. The spray symmetry was also investigated using the time-averaged water volume fraction. The analysis revealed asymmetrical spray patterns downstream of the nozzle. This asymmetry in the distribution of droplets suggests potential challenges in achieving uniform spray coverage.

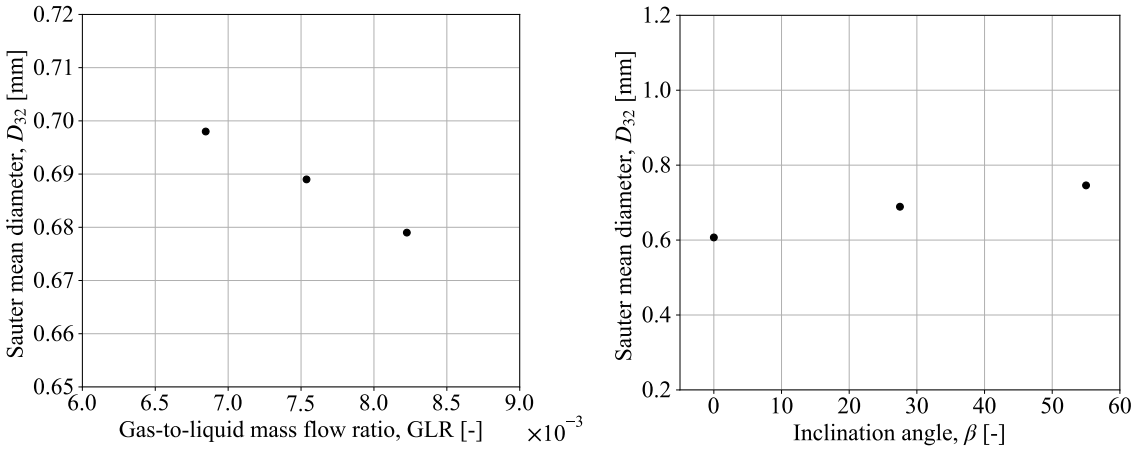

Figure 1: The figures show the Sauter mean diameter, D_{32}, as a function of both the GLR and the inclination angle of the inlet pipes.

In this study, three inclination angles of 0 °, 27.5 °, and 55 ° have been investigated and the results of the simulations are presented in Figure 1b. The SMD decreased by 11.9 % with an inclination angle of 0 ° compared to the baseline case of 27.5 °. When the inclination angle increased to 55 °, the SMD increased by approximately 8.3 %. The result might be attributed to the increased turbulent mixing inside the nozzle with an inclination angle of 0 °, which would enhance the atomization process.

Furthermore, the spray symmetry was investigated for each of the inclination angles. The results can be seen in Figure 2, where the time-averaged volume fraction of water is visualised. The contour was plotted downstream of the nozzle orifice at a distance corresponding to one orifice diameter, $1D$. The least symmetrical spray was achieved with an inclination angle of 27.5 °, while an angle of 0 ° and 55 ° produced slightly more symmetric sprays. Furthermore, the region with the highest α values was seen to shift for an inclination angle of 55 °. Based on the findings in this study, the most optimal design was determined to be an inclination angle of 0 ° due to the improved spray symmetry and lowest SMD.

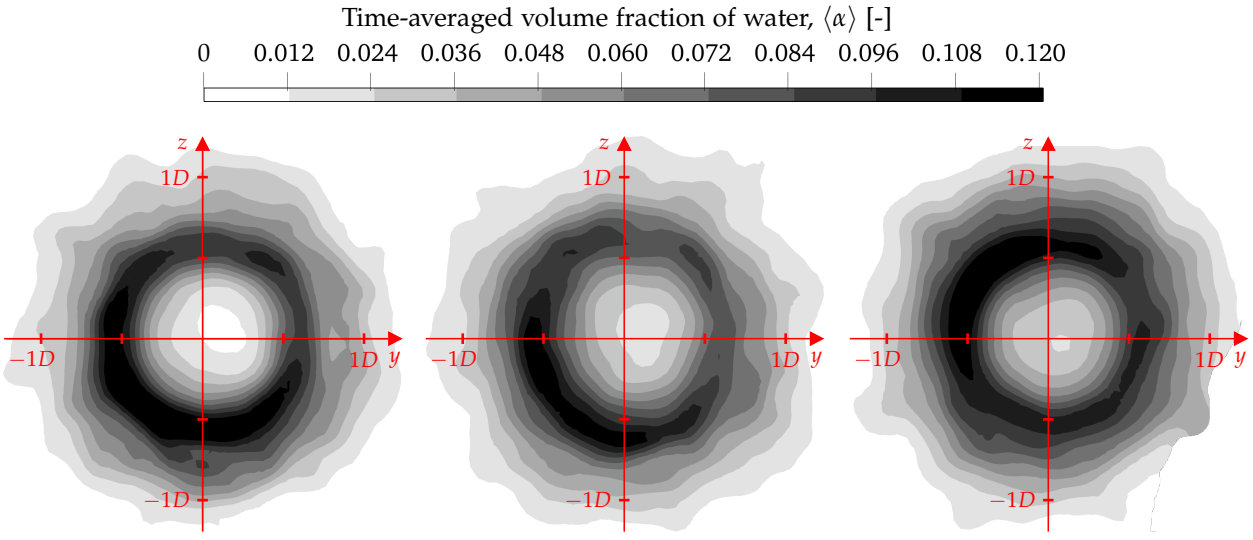

(a) $\beta = 0$ °

(b) $\beta = 27.5$ °

(c) $\beta = 55$ °

Figure 2: The figures show the contour plot of the time-averaged volume fraction of water for the investigated inclination angles at a distance of $1D$ downstream of the nozzle orifice.

Abbreviations

Abbreviation	Definition
CFD	Computational fluid dynamics
DNS	Direct numerical simulation
GCI	Grid convergence index
GLR	Gas-to-liquid mass flow ratio
LES	Large Eddy Simulation
PDF	Probability density function
RANS	Reynolds-averaged Navier-Stokes
RNG	Re-normalisation group
SGS	Sub-grid scale
SMD	Sauter mean diameter
VoF	Volume of Fluid
WALE	Wall-adapting local eddy-viscosity

Nomenclature

Symbol	Definition	Unit
B	Impact parameter	-
d	Droplet diameter	m
D	Orifice / inlet pipe diameter	m
D_{10}	Arithmetic mean droplet diameter	m
D_{32}	Sauter mean diameter	m
f	Arbitrary data point	-
f_{PDF}	Probability density function	-
f_0	Arbitrary ideal value	-
f_0^+	Top error band	-
f_0^-	Bottom error band	-
F_s	Safety factor	-
$\boldsymbol{g}$	Gravitational acceleration	$\mathrm{m/s^2}$
I	Turbulence intensity	-
$\dot{m}$	Mass flow rate	kg/s
n	Arbitrary variable	-
$\boldsymbol{n}$	Normal vector	-
N	Number of a given variable	-
O	Order of convergence	-
p	Pressure	Pa
$\dot{Q}$	Volume flow rate	$\mathrm{m^3/s}$
r	Local radial distance	m
R	Pipe radius	m
Re	Reynolds number	-
$\boldsymbol{s}$	Skewness vector	-
$\boldsymbol{S}$	Source term	-
t	Time	s
t^*	Normalised time	-
$\boldsymbol{u}$	Velocity vector	m/s
V	Volume	$\mathrm{m^3}$
We	Weber number	-
x	x-direction	-
y	y-direction	-
y^+	Dimensionless first cell height	-
z	z-direction	-

Symbol	Definition	Unit
α	Volume fraction	-
β	Inclination angle of the inlet pipes	-
γ	Grid refinement ratio	-
δ	Distance	m
ϵ	Relative error	-
κ	Curvature	m^{-1}
θ	Non-orthogonality angle	-
μ	Dynamic viscosity	Pa· s
μ	Sample mean	-
ρ	Density	kg/m^3
σ	Surface tension	N/m
σ	Standard deviation	-

Subscript and Superscript

Symbol	Definition
1	fine
2	medium
3	coarse
c	cell-centred value
d	droplets
D	depth
g	gas
H	height
i	i'th entry
l	liquid
L	length
max	maximum
min	minimum
sgs	sub-grid scale
σ	surface tension
x	x-direction
y	y-direction
z	z-direction

Operators

Symbol	Definition
$\overline{x}$	A filtered variable
x'	A fluctuating variable
$\langle x \rangle$	A time-averaged variable

Table of Contents

1 Introduction

Droplet atomization processes are used extensively in several areas such as fuel injection, spray painting, and gas cooling. The design of a nozzle, therefore, depends on the application it is to be used for. The most widely used nozzle concept is the single-fluid nozzle, where a pressurised liquid is forced through a specifically shaped chamber and orifice (Tian 2019). The nozzles are designed to atomize the liquid, which is achieved through the increase in the liquid velocity, as it is forced through the nozzle orifice. Furthermore, it is possible to create different spray patterns depending on the single-fluid nozzle design. In Figure 1.1, the simple single-fluid plain-orifice and shaped-orifice nozzle are presented. The plain-orifice nozzle produces a jet of droplets, whereas the shaped-orifice nozzle creates a flat fan spray (Ashgriz 2011).

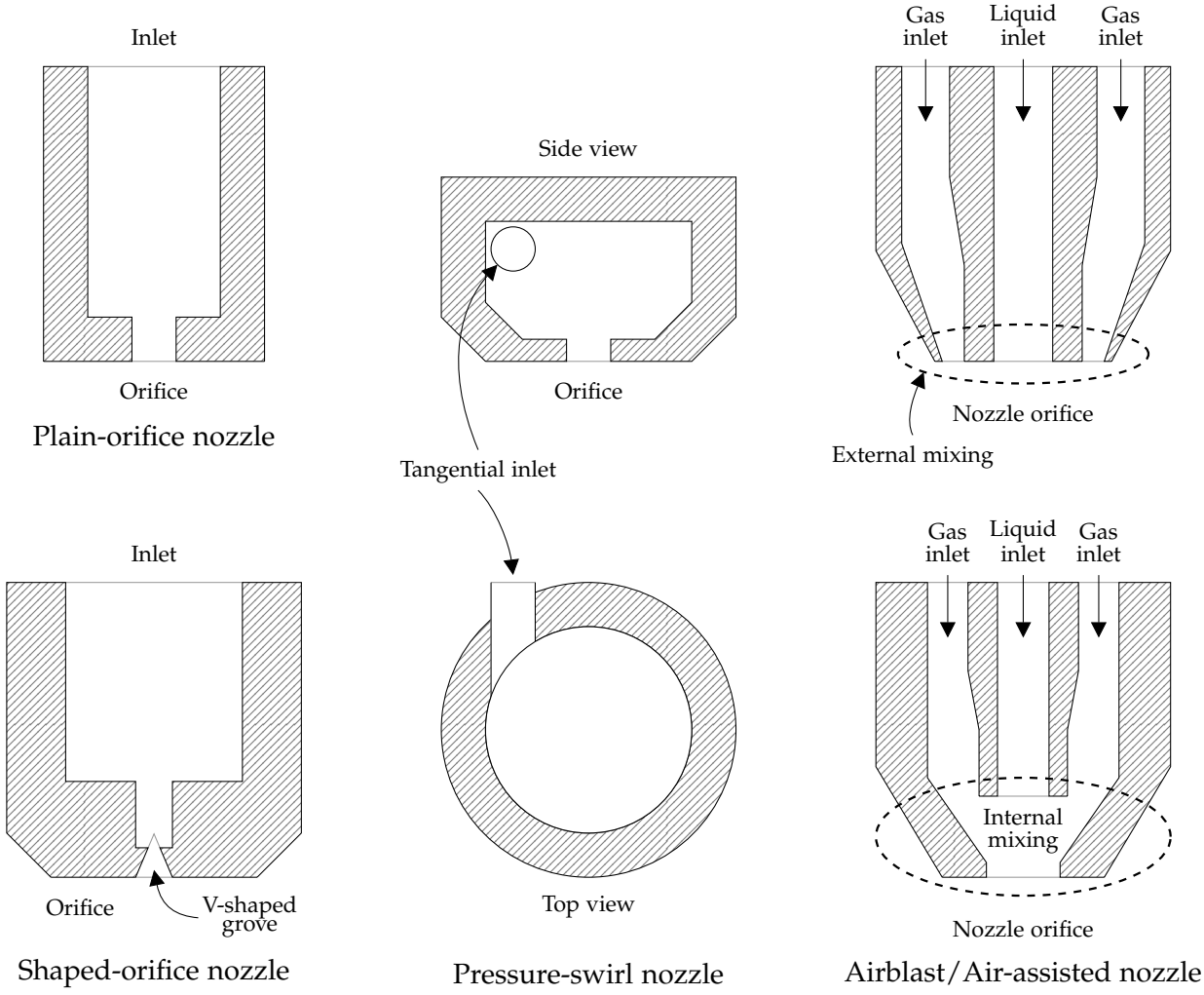

Figure 1.1: Different nozzle geometries and designs (Tian 2019).

One of the most commonly used nozzle types is the pressure-swirl nozzle, which comes in many different designs. The designs generally vary between having an axial or tangential inlet flow of the fluid which is to be atomized. The pressure-swirl nozzle with an axial inlet flow configuration requires special vanes or groves to swirl the liquid. However, it is often necessary to incorporate an auxiliary fluid to help atomize the liquid. In Figure 1.1, a sketch of a simple pressure-swirl nozzle with a tangential inlet channel is presented. The tangential inlet flow facilitates the atomization of the liquid due to the centrifugal force acting on the liquid and the fast-swirling motion which eliminates the need for an auxiliary fluid (Ashgriz 2011). However, pressure-swirl nozzles are often operated as twin-fluid nozzles, where a liquid and a gas are used (Ashgriz 2011). In the tangential inlet flow configuration, injection of both the liquid and gas in the same direction enhances the swirl motion of the fluids. An opposite injection direction between the liquid and gas instead creates opposing shear forces which enhances the mixing and thereby the atomization (Ashgriz 2011).

In Figure 1.1, the airblast/air-assisted nozzle configurations are presented as examples of twin-fluid nozzles. A twin-fluid nozzle is internally mixing if the gas and liquid are brought in contact within the nozzle, or externally mixing if brought in contact outside the nozzle. An important parameter used to describe twin-fluid nozzles is the gas-to-liquid mass flow ratio (GLR), which is given as:

$$\mathrm{GLR} = \frac{\dot{m}_\mathrm{g}}{\dot{m}_\mathrm{l}} \tag{1.1}$$

where $\dot{m}$ is the mass flow rate and the subscripts g and l denote gas and liquid respectively. The airblast/air-assisted nozzle design commonly consists of an inner liquid-carrying tube surrounded by an annular gas flow tube. The main distinction between airblast and air-assisted nozzles lies in the required operating conditions. For the airblast nozzle configuration, high GLRs are used to achieve atomization, and the air is supplied continuously (Ashgriz 2011). The air-assisted nozzle configuration is operated with low GLRs, and the air is pressurised and supplied when needed.

Twin-fluid nozzles are available in multiple designs, however, among the most studied designs is the internally mixing Y-jet nozzle. The naming is due to the characteristic Y-mixing ports, where the gas and liquid first come into contact before leaving the multiple nozzle orifices. This nozzle type is commonly operated with a high GLR. A high relative velocity is achieved between the gas and liquid, which results in the formation of small droplets. Furthermore, the high relative velocity promotes good liquid dispersion and prevents droplet coalescence (Nazeer et al. 2020).

1.1 State of the Art on Twin-Fluid Nozzles

Several studies have investigated droplet size distribution experimentally using twin-fluid nozzles. The study by Zhou et al. (2010) experimentally investigated the atomization performance of a single-hole Y-jet nozzle, and found that the mean droplet diameter decreased as the GLR increased. Watanawanyoo et al. (2011) designed and experimentally investigated a twin-fluid atomizer for a fuel injection system. It was found that increasing the GLR moved the point of the initial breakup closer to the nozzle exit while decreasing the GLR moved it further downstream of the nozzle exit. In terms of nozzle design, Lee et al. (2023) experimentally tested elliptical nozzles in comparison to a standard circular nozzle, and the study showed a more asymmetrical spray pattern with the elliptical nozzle. Ochowiak (2016) conducted experiments on a conical internal mixing twin-fluid swirl nozzle and found that increasing the mixing-chamber length resulted in larger droplets, whereas higher GLR resulted in smaller droplets. The study by Barbieri et al. (2023) experimentally investigated the effect of geometric variations on an internal mixing Y-jet nozzle. Smaller droplet sizes were achieved when the internal mixing chamber length decreased. A narrower Y-impingement angle between the gas and liquid had the same effect.

Numerical analysis is a powerful tool for studying atomization, as an alternative to the often expensive and time-consuming process of constructing an experimental setup. Several studies have been carried out using CFD with the Reynolds Averaged turbulence approach to study twin-fluid atomization.
The study by Ludwig et al. (2022) conducted CFD simulations on a pneumatic nozzle using an Euler-Lagrange approach with the Discrete Phase Model (DPM). The CFD simulations were compared with experimental data to find the most suitable Reynolds-averaged turbulence model. The most accurate model was the standard $k-\epsilon$, which had a relative error of 10.5 % compared to the experimental velocity of the dispersed phase. Liu et al. (2022) investigated a pneumatic nozzle design using the Euler-Lagrange DPM with the realizable $k-\epsilon$ turbulence model. A higher gas pressure was found to decrease the droplet size. Mohammadi et al. (2022) studied atomization characteristics and droplet size distribution of an internal mixing atomizer both experimentally and numerically using the RNG $k-\epsilon$ turbulence model. The authors reported that reasonable agreement was found between the numerical and experimental results in terms of spray cone angle, droplet size distribution, and velocity. The study by Han et al. (2020) investigated the effect of liquid inlet pressure on the droplet size distribution and velocity. The simulations were conducted using the volume of fluid (VoF) method with the RNG $k-\epsilon$ turbulence model. As the liquid supply pressure increased, the droplet size and velocity increased.

The Reynolds Averaged turbulence approach generally has the advantage of low computational cost. However, the computationally intensive large eddy simulation (LES) approach is able to capture the unsteady flow dynamics, which play an important role in studies of twin-fluid atomization (Trautner et al. 2023).
Zhang et al. (2023) conducted a numerical and experimental study on an external mixing nozzle to investigate the impact of varying gas injection angles on the atomization process. The primary breakup of the liquid jet was simulated numerically using the VoF method. LES was used to model turbulence with the wall-adapted local eddy-viscosity (WALE) sub-grid scale (SGS) model. Increasing the gas injection angle from 0° to 30° resulted in a shorter liquid core length due to the higher gas flow velocity. The atomization process of an internal mixing Y-jet atomizer was numerically studied by Nazeer et al. (2020). LES was carried out using the Smagorinsky SGS model and a VoF to DPM approach. A higher GLR was found to reduce the droplet size. Hua et al. (2024) simulated the primary breakup of molten metal using a VoF to DPM approach, where the VoF method simulated the primary breakup and DPM tracked the secondary breakup. LES with the WALE SGS model was used as the large eddies interact with droplets and affect the breakup and droplet size distribution. It was found that higher gas pressure, lower viscosity, or lower surface tension lead to the formation of smaller droplets in the atomization process. The effect of liquid flow rate was investigated by Chen et al. (2022) using the VoF to DPM approach. LES was carried out to simulate the atomization process of a twin-fluid nozzle. The results showed an increase in droplet size with decreasing GLR.

The literature review above provides an overview of the current knowledge in the field of twin-fluid atomization. The present study aims to investigate the droplet formation of a twin-fluid nozzle using CFD simulations. The different multiphase and turbulence modelling approaches will be presented in the following.

2 Problem Statement and Description

Understanding and accurately predicting turbulent multiphase flows is of great importance in the field of atomization. The complexity in multiphase flows arises from the interactions between different phases, e.g. phase separation and interfacial dynamics. These interactions significantly influence the flow behavior, mixing, and mass transfer in a system. Several multiphase and turbulence models have been developed in the literature. In this chapter, the major models will be compared, and the most suitable will be selected and used throughout this study.

2.1 Multiphase Modelling

Different approaches can be taken to model multiphase flows. One approach is the Euler-Euler method, where the flow field is considered continuous across the whole domain. The second is the Langrangian method, where individual particle or droplet paths are tracked throughout the domain. In the Euler-Lagrange approach, the fluid is treated as a continuous phase and the individual particles or droplets move through the flow field. Their trajectories are determined from the forces acting on them (Basha et al. 2019). The dispersed phase particles or droplets are often present at low volume fractions (Lain and Sommerfeld 2003). In the Euler-Lagrange approach, the discrete phase must be supplied at a given particle diameter, which may not be known beforehand.

The Euler-Euler method can be categorized into different sub-models, i.e. the volume of fluid (VoF) method and the Eulerian model. The Eulerian model is designed for two or more phases which are treated as interpenetrating continua meaning the phases can share a cell in the computational domain simultaneously. The exact location of the interface in the cell is not tracked in this model, which means additional sub-models are needed to determine the size of the droplets (Basha et al. 2019). Decisions must be made in terms of sub-models before simulating how the droplets form. The VoF method assumes that the phases share a single velocity field and do not interpenetrate. Properties such as density and viscosity are averaged between the phases, which means it is necessary to avoid smearing the interface due to a low mesh resolution. This means a high mesh resolution is required to ensure the volume fraction between the two phases transitions from 0 to 1 over ideally three cells.
The comparison between the VoF and Eulerian model is visualised in Figures 2.1 and 2.2. It shows how the VoF method requires a finer mesh to capture the free surface of the droplets, whereas the exact interface and location of the droplets are not captured when using the Eule-

rian model. Instead, the droplets are simply represented by a volume fraction. The VoF method is computationally expensive, but the sharp interface makes it suitable for predicting the atomization process. The VoF method is advantageous as the droplet size distribution is determined directly by the physics of the simulation and not from predefined sub-models. It is therefore a suitable choice of multiphase model when the droplet size distribution is unknown beforehand.

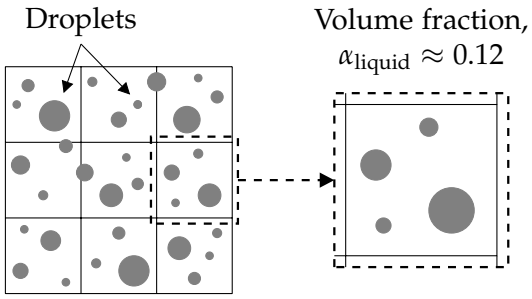

Figure 2.1: Visualisation of how the droplets are represented by a volume fraction in the Eulerian model. The location and interface of the droplets are not tracked (Basha et al. 2019).

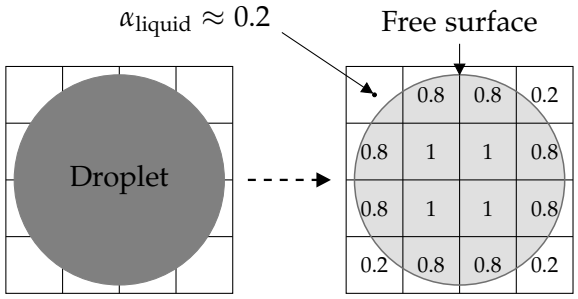

Figure 2.2: Visualisation of how the location and free surface of the droplets are tracked using the volume of fluid model (Basha et al. 2019).

Based on the overview of the different models, the VoF model is most appropriate for the application in this study. This approach allows the simulation to resolve the formation, breakup, and coalescence of droplets based on the underlying physics of the flow. Consequently, the droplet size distribution emerges directly from the simulation due to factors such as fluid velocity, turbulence, surface tension, and interaction with the nozzle geometry.

2.2 Turbulence Modelling

The three approaches to simulating turbulence in CFD are direct numerical simulations (DNS), large eddy simulations (LES), and Reynolds-averaged Navier-Stokes (RANS). These differ in terms of the time and length scales directly resolved in the flow field.

Unsteady three-dimensional turbulent flows are characterised by eddies having a wide range of length scales. The largest eddies are often comparable in size to the flow domain, while the smallest eddies and length scales are responsible for the dissipation of turbulent kinetic energy. Without introducing any model, the DNS method directly solves the Navier-Stokes and continuity equation numerically for the whole spectrum of length scales. This means that the numerical mesh must be smaller than the smallest eddies dissipating the turbulent kinetic energy. However, DNS is often not a feasible choice of turbulence model in practical engineering problems, as the computational expense would be prohibitive (Rodi 2006). As shown in Figure 2.3, the LES

approach directly solves flow structures larger than the grid size, while a sub-grid scale (SGS) model accounts for the influence of eddies smaller than the grid size. The approach can therefore be very computationally expensive when working with three-dimensional, highly turbulent, wall-bounded, and viscous flows, though not to the same extent as DNS (Nazeer et al. 2020).

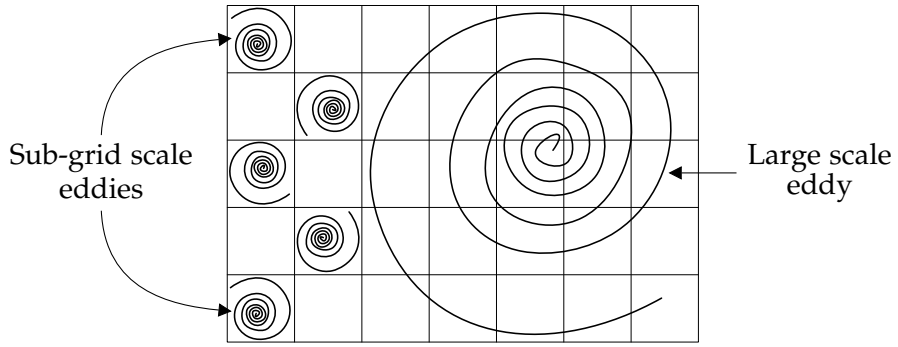

Figure 2.3: Visualisation of the resolved and modelled eddies in a large eddy simulation.

In the RANS approach, the starting point is the Reynolds decomposition of the flow variables into mean and fluctuating components as shown below for the instantaneous velocity:

$$\boldsymbol{u} = \boldsymbol{u}' + \boldsymbol{u}_{\text{mean}} \tag{2.1}$$

The mean component, $\boldsymbol{u}_{\text{mean}}$, represents the average velocity over time, and the fluctuating component, $\boldsymbol{u}'$, represents the turbulent fluctuations around the mean. These Reynolds-decomposed flow variables are inserted into the Navier-Stokes equations which are averaged to filter out the velocity fluctuations due to turbulence. The decomposition gives rise to the Reynolds stress tensor in the RANS equations. This has to be modelled to close the system of equations. The Reynolds stress tensor contains information about the direction and magnitude of the momentum exchange between different parts of the flow due to turbulent fluctuations (Nazeer et al. 2020).

The VoF-LES method combines the accurate interface capturing capabilities of the VoF approach while resolving large turbulent structures using LES. LES is more suitable for studying the atomization process compared to the RANS approach, which relies on turbulence models to parameterize turbulent effects.

2.3 Problem Statement

This study aims to numerically investigate and quantify the droplet size distribution from an internal mixing twin-fluid swirl nozzle. Only low Reynolds number flows will be considered to reduce computational cost. The focus will be on assessing the dependence of key parameters such as nozzle geometry and operating conditions on the droplet size distribution. This leads to the following problem statement:

How can an internal mixing twin-fluid swirl nozzle be modelled using a VoF-LES approach to predict the droplet size distribution?

2.4 Problem Description

In this study, a swirl nozzle based on the design proposed by Ochowiak (2016) is used. Figure 2.4 presents both a cross-sectional and top view of the nozzle design. The working fluids enter through different inlet pipes before reaching the conical mixing chamber. The diameter, D, of both inlet pipes and the nozzle outlet is 2.5 mm and the inclination angle, β, is 27.5 °. The conical shape and inclination angle create the swirling motion inside the nozzle, which decreases the axial velocity, and thereby increases the duration over which the water and air interact.

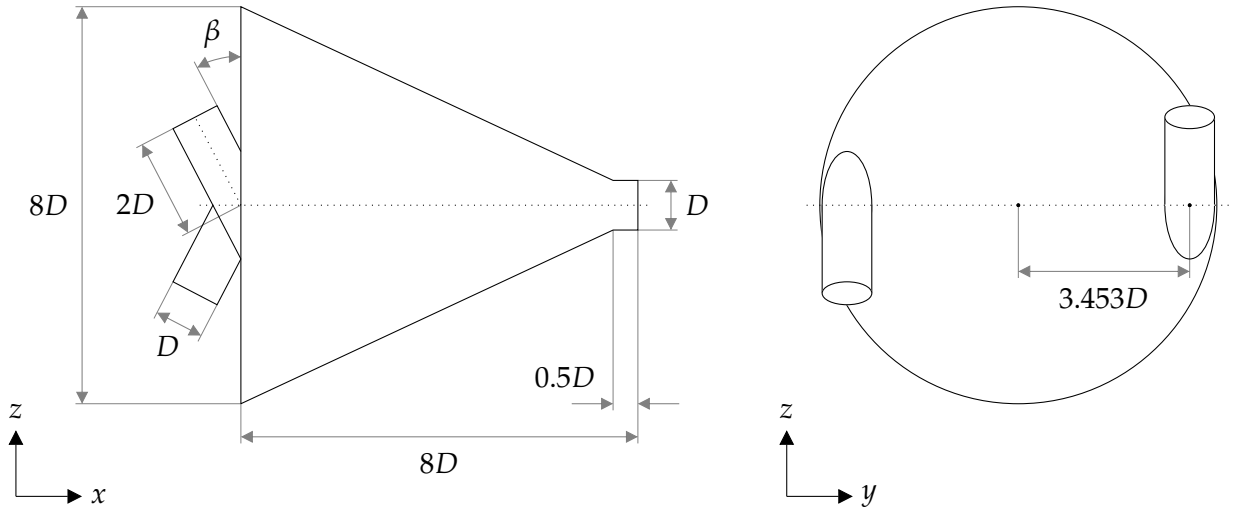

Figure 2.4: Schematic of the internal mixing twin-fluid swirl nozzle design proposed and used by Ochowiak (2016).

A numerical study will be conducted based on a CFD model, where the meshing process will be carried out in the software ANSYS Fluent and the simulations in OpenFOAM. This will be validated with the experimental data from the study by Ochowiak (2016). The experimental tests were conducted with water and air as the working fluids at a temperature of 293 $\pm$ 1 K. The physical properties of the working fluids used in the simulations in this study are presented in Table 2.1. Due to the low Reynolds numbers in the experiments, the gas is assumed to be incompressible in the CFD model.

Table 2.1: Physical properties of the working fluids used in the simulations in this study.

Properties	**Water**	**Air**
Density [kg/m^3]	1000	1.293
Kinematic viscosity [m^2/s]	$1.0{\cdot}10^{-6}$	$1.48{\cdot}10^{-5}$
Surface tension [N/m]	0.0738	
Reynolds number [-]	5650	1980
Bulk velocity [m/s]	2.27	12

In the experiments conducted by Ochowiak (2016), the author has failed to provide key information regarding:

- The distance downstream of the nozzle where the droplet size distribution was obtained.
- The time duration between the initial and final droplet size measurements.
- Whether the inlet flow of the two working fluids was fully developed before entering the conical mixing chamber.
- The specific inclination angle of the inlet pipes.

Between the two first points of missing information, the choice of the distance downstream of the nozzle is expected to affect the droplet size distribution to the greatest extent. Two downstream distances will therefore be investigated to come as close to the experimentally determined droplet size distribution as possible. The length of the time interval over which the droplet size distribution is measured mainly affects the statistical mean droplet size distribution. A brief study will be conducted to determine the time dependency of parameters such as velocity and droplet size to estimate an appropriate simulation time. Regarding the two last points of missing information, the inlet flow of both working fluids is assumed to be fully developed. Furthermore, the inclination angle has been measured from a system sketch in the study by Ochowiak (2016). However, the proportions of the sketch do not entirely match the listed measurements of the nozzle.

2.4.1 Structure of the Report

To give the reader an overview of the structure of the report, a brief description of the content of each chapter is presented here.

- Chapter 3 presents the dimensionless numbers used to characterise the swirl nozzle. Furthermore, the internal and external flow patterns are described for single and twin-fluid atomizers. Lastly, the fundamental theory of droplet separation and coalescence is presented.
- Chapter 4 presents the governing equations and numerical theory used to model the droplet atomization process. Additionally, the chapter contains a description of the computational domain used for the CFD simulations.
- Chapter 5 presents a time and mesh independence study followed by the validation of the CFD model with experimental data.
- Chapter 6 presents the results obtained by the CFD simulations in terms of varying the GLR and assessing the spray symmetry. Furthermore, the effect of varying the inclination angle of the inlet pipes is investigated.

3 Single and Twin-Fluid Atomization

This chapter presents relevant theory on the subject of single and twin-fluid atomization from the literature. Specifically, the internal flow in the nozzle as well as the primary break-up mechanisms downstream of the nozzle will be described. The dimensionless numbers used throughout the study to describe flow characteristics will be presented first.

3.1 Dimensionless Numbers

This section presents the dimensionless numbers used throughout this study to reduce the number of variables to simplify the analysis and normalise certain parameters. One of the most fundamental dimensionless numbers in fluid mechanics is the Reynolds number, Re, which represents the ratio of inertial forces to viscous forces as shown below:

$$\mathrm{Re} = \frac{\rho u_{\mathrm{bulk}} D}{\mu} \tag{3.1}$$

where ρ is the fluid density, u_{bulk} is the bulk velocity, D is the pipe diameter, and μ is the dynamic viscosity.

As previously described, an important parameter used to describe twin-fluid nozzles is the gas-to-liquid mass flow ratio (GLR), which is given as:

$$\mathrm{GLR} = \frac{\dot{m}_{\mathrm{g}}}{\dot{m}_{\mathrm{l}}} \tag{3.2}$$

where $\dot{m}$ is the mass flow rate and the subscripts g and l denote gas and liquid respectively.

The dimensionless Weber number, We, represents the ratio of the inertial forces to the surface tension forces and is defined as:

$$\mathrm{We} = \frac{\rho d u_{\mathrm{droplet}}}{\sigma} \tag{3.3}$$

where d is the droplet diameter, u_{droplet} is the droplet velocity and σ is the surface tension of the liquid. It is used in the relevant theory on droplet separation and coalescence.

To characterise the simulation time, the normalised time, t^*, is introduced and used in later chapters. It describes the number of times the air inside the nozzle has been replenished is given

by:

$$t^* = \frac{\dot{Q}_{\text{air,bulk}}}{V_{\text{air}}} t \tag{3.4}$$

where $Q_{\text{air,bulk}}$ is the volumetric flow rate of the bulk airflow at the inlet, V_{air} is the volume of the air contained inside of the nozzle, and t is the time.

The turbulence intensity is introduced to describe the shear stress between the working fluids in the later chapters. The turbulence intensity, I, is defined as the ratio between the fluctuating component of the velocity and the mean component as shown below (Basse 2017):

$$I = \frac{\sqrt{(u'_{\text{x}})^2 + (u'_{\text{y}})^2 + (u'_{\text{z}})^2}}{u_{\text{bulk}}} \tag{3.5}$$

where u' represents the turbulent velocity fluctuations in each spatial direction and u_{bulk} is the mean velocity, which is calculated as the mean velocity directly at the nozzle exit.

3.2 Internal Flow in Single-Fluid Swirl Nozzle

In a converging single-fluid swirl nozzle configuration with tangential inlet channels, the liquid forms a rotating flow inside the nozzle chamber as presented in Figure 3.1. At higher inlet liquid flow rates, a conical swirling sheet is formed downstream of the nozzle orifice due to the swirling motion and kinetic energy of the liquid inside the nozzle chamber (Ashgriz 2011). As the conical liquid sheet spreads outwards, it becomes thin and eventually breaks into small droplets.

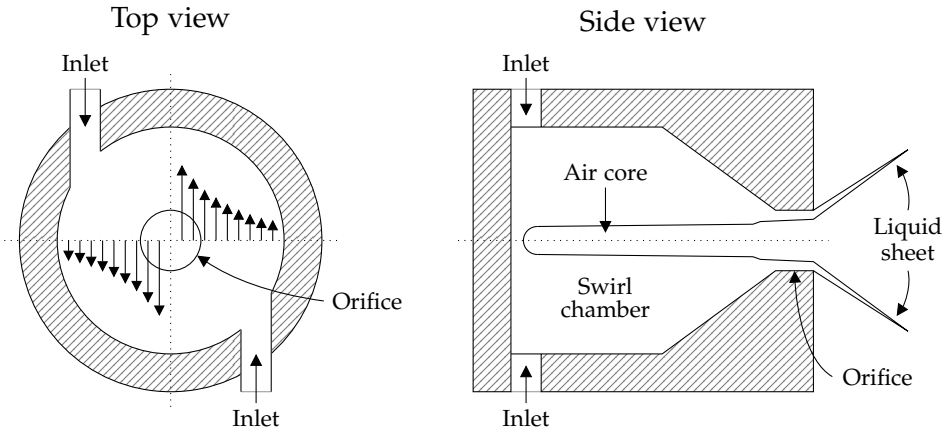

Figure 3.1: Schematic of the air core formed inside a converging single-fluid swirl nozzle with tangential inlet channels (Ashgriz 2011).

The rate of the inlet liquid flow determines whether an air core is formed through the outlet

nozzle orifice and inside the nozzle chamber as described by Ashgriz (2011). The air core develops if a critical Reynolds number is exceeded for the liquid flow. Below this critical Reynolds number, a full jet will exit the nozzle orifice to produce a solid cone spray. The size of the air core increases with increasing liquid inlet flow rate. As the liquid inlet flow rate increases, a second critical Reynolds number is reached where the air core becomes fully developed and takes a cylindrical shape inside the nozzle chamber. The air core retains its cylindrical shape throughout the cylindrical and converging part of the nozzle chamber and only expands at the entrance of the nozzle orifice. The liquid film in the orifice becomes thinner as the diameter of the air core increases, which produces smaller droplets. The droplet size distribution is therefore highly affected by the presence of the air core and its geometric and turbulent characteristics.

3.3 Spray Formation from Twin-Fluid Atomizer

In an internal mixing twin-fluid atomizer, the formation of the spray begins inside the nozzle. The internal flow determines how the liquid disintegrates and how the spray develops in time and space. The type of internal flow depends mainly on the GLR. As the GLR increases, and consequently also the gas mass flow, the thickness of the liquid film in the circumference of the orifice is reduced (Zaremba et al. 2017). Instabilities caused by shear stress develop into waves on the surface of the liquid film. As the waves grow, they eventually break off from the liquid core and form droplets (Nazeer et al. 2020). During this process, the gas phase transfers kinetic energy to the liquid through the shear stress. The detaching of the liquid core into ligaments or large droplets is called primary breakup and is seen in the dense spray region in Figure 3.2. The ligaments and large droplets can break up into smaller droplets through interactions with the ambient gas and droplet collisions, which is called secondary breakup and is seen in the dilute spray region (Watanawanyoo et al. 2012).

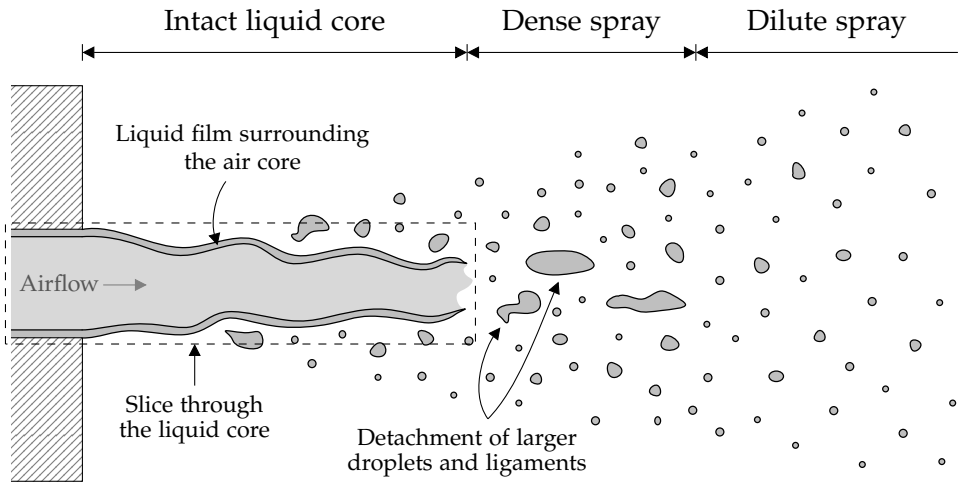

Figure 3.2: Visualisation of the process of droplets and ligaments detaching from the liquid core at the nozzle exit.

3.4 Droplet Separation and Coalescence

In a study on liquid droplets by Ashgriz (1990), four primary outcomes of binary droplet collision are presented, which are bouncing collision, permanent coalescence, temporary coalescence with later separation, and shattering collision. The bouncing collision occurs due to a trapped gas layer at the interface between the two droplets approaching each other. Under certain conditions, the compressed gas layer prevents contact between the droplet surfaces, leading to deformation and the droplets bouncing off each other. Coalescence can be a permanent or temporary phenomenon, and in the latter case, the coalesced initial droplets separate into a string of two or more droplets. This is due to the inertial force dominating compared to the surface tension force and viscous dissipation, which instead promote coalescence. In the case of high relative velocities between the droplets, shattering collisions can occur where the two droplets disintegrate into a cluster of smaller droplets.

The droplet collision sequence resulting in separation can be divided into three periods seen in Figure 3.3. In the first period, two droplets collide head-on and form an outwardly spreading disk. In the second period, the disk contracts due to the surface tension and the internal fluid flows inward. In the third period, a stretched liquid cylinder is formed with the internal fluid flowing outward, which produces a thin inter-connecting ligament. If the initial kinetic energy of the liquid droplets is large enough to overcome the viscous dissipation, the ligament breaks, and if not, the surface tension will oppose separation and seek to minimise the surface area to a spherical shape (Qian 1997).

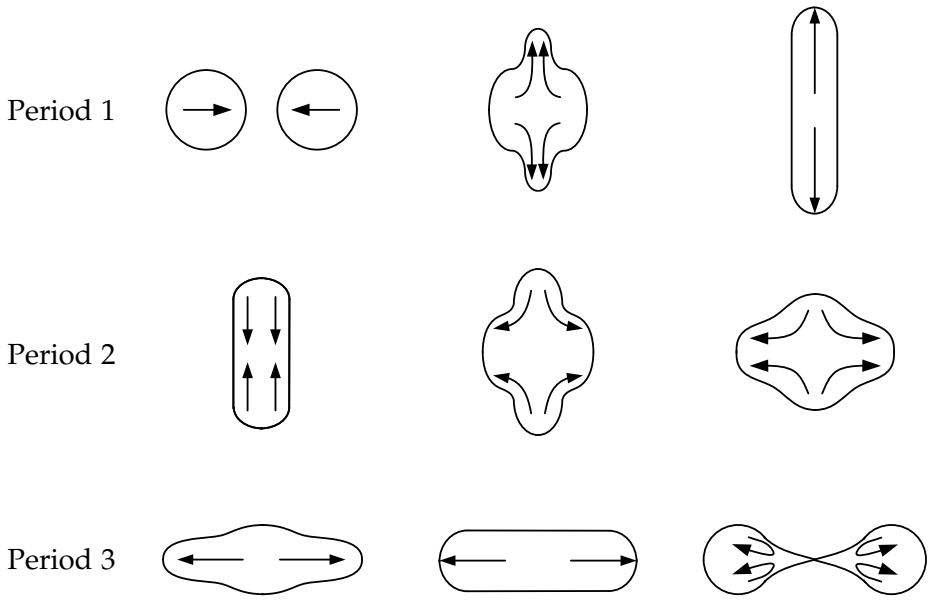

Figure 3.3: Visualisation of the three periods of head-on droplet collision and separation (Qian 1997).

A later study by Qian (1997) further presents the outcome of binary droplet collisions as a function of the Weber number and an impact parameter for both water and hydrocarbon droplets. The impact parameter, B, defined by Qian (1997) designates whether the droplets collide head-on ($B = 0$) or only graze each other ($B = 1$). In Figure 3.4, the droplet collision regimes are presented for water and hydrocarbon droplets in airflow at atmospheric pressure respectively.

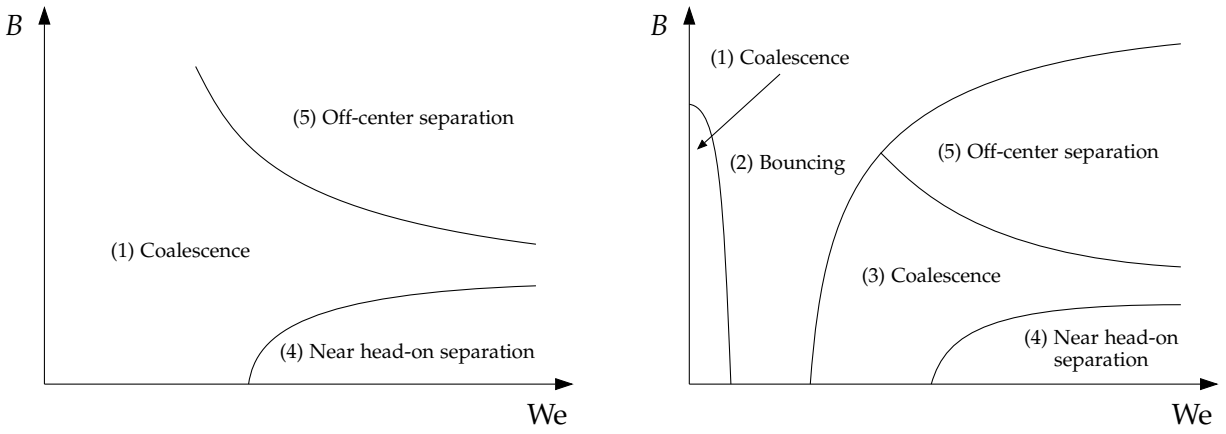

(a) Water droplets in airflow.

(b) Hydrocarbon droplets in airflow.

Figure 3.4: Collision regime diagrams for water and hydrocarbon droplets in air at atmospheric pressure, where the impact parameter, B, designates whether the droplets collide head-on ($B = 0$) or only graze each other ($B = 1$) (Qian 1997).

Specifically for water droplets, the bouncing collision is not observed, which might be explained by the higher surface tension and lower viscosity of water compared to hydrocarbons (Qian 1997). Coalescence is instead facilitated for water droplets under these conditions. The lower viscosity means lower viscous dissipation, resulting in a larger portion of the initial kinetic energy available for the droplets to overcome surface tension forces (Qian 1997). The surface tension force which dominates for water droplets also promotes coalescence, as the surface tension aims at minimising the surface area and therefore pulls adjacent water molecules together. Furthermore, water droplets experience relatively small surface deformation due to the lower viscosity, which means that two collided droplets more readily return to a spherical shape (Qian 1997).

4 Numerical Approach to Simulating Atomization

This chapter outlines the numerical approach to simulating the turbulent multiphase flow within an internal mixing twin-fluid swirl nozzle and the downstream atomization. The governing equations that describe the dynamics of turbulent multiphase flows are presented, followed by a description of the volume of fluid (VoF) method. Furthermore, the computational domain and boundary conditions are presented. The chapter concludes with a description of the mesh topology and initialisation process.

4.1 Governing Equations

The large eddy simulation (LES) method resolves the large eddies in the computational domain and then models the influence of the smaller eddies. A filtering operation is used to separate the large and small eddies. The governing equations will be described in the following.

In the VoF formulation, a single momentum equation is solved, and the resulting velocity field is shared among the phases. The volume fractions of the two phases are accounted for through the density, ρ, and viscosity, μ (Shrestha et al. 2023). The Navier-Stokes continuity and momentum equations for incompressible fluid flow are shown below.

$$\nabla \cdot (\rho \overline{\boldsymbol{u}}) = 0 \tag{4.1}$$

$$\underbrace{\frac{\partial(\rho \overline{\boldsymbol{u}})}{\partial t}}_{\substack{\text{Rate of change} \\ \text{of velocity}}} + \underbrace{\nabla \cdot (\rho \overline{\boldsymbol{u}}\overline{\boldsymbol{u}})}_{\text{Convective flux}} = \underbrace{-\nabla \overline{p}}_{\substack{\text{Pressure} \\ \text{gradient}}} + \underbrace{\rho \boldsymbol{g}}_{\substack{\text{Gravitational} \\ \text{effect}}} + \underbrace{\nabla((\mu + \mu_{\text{sgs}})\nabla \cdot \overline{\boldsymbol{u}})}_{\text{Diffusive flux}} + \underbrace{\boldsymbol{S}_\sigma}_{\substack{\text{Surface} \\ \text{tension}}} \tag{4.2}$$

where $\overline{\boldsymbol{u}}$ is the filtered mixture velocity shared by the phases, $\overline{p}$ represents the filtered pressure field, $\boldsymbol{g}$ is the gravitational acceleration. The diffusive flux accounts for the sub-grid scale (SGS) eddy viscosity, μ_{sgs}. The eddy viscosity part arises due to the filtering operation to account for eddies that are smaller than the cells in the domain (Versteeg and Malalasekera 2007). The source term, $\boldsymbol{S}_\sigma$, accounts for the surface tension force which tends to pull the liquid into the form of a sphere, since this geometry has minimum surface energy (Nazeer et al. 2020). Surface tension contributes a surface pressure, which is modelled as a continuum surface force using the approach proposed by Brackbill et al. (1992). The interface between the two phases is regarded

as a transition region of a finite thickness defined by the grid spacing as visualised in Figure 4.1. The surface tension source term is modelled as seen below:

$$\boldsymbol{S}_\sigma = \sigma\kappa\nabla\alpha_c \tag{4.3}$$

where σ is the surface tension, α_c is the cell-centred volume fraction of liquid, and κ is the curvature of the interface given by the divergence of the interface normal vector, $\boldsymbol{n}$, as shown in Equation 4.4. The term, $\nabla\alpha_c$, ensures that the surface tension effect is only accounted for at the interface between the phases, since the gradient is zero everywhere else.

$$\boldsymbol{n} = -\frac{\nabla\alpha_c}{|\nabla\alpha_c|}, \qquad \kappa = -\nabla\boldsymbol{n} \tag{4.4}$$

This means that in convex and concave regions, the force acts to flatten the surface resulting in a smooth and stable interface with minimum surface area.

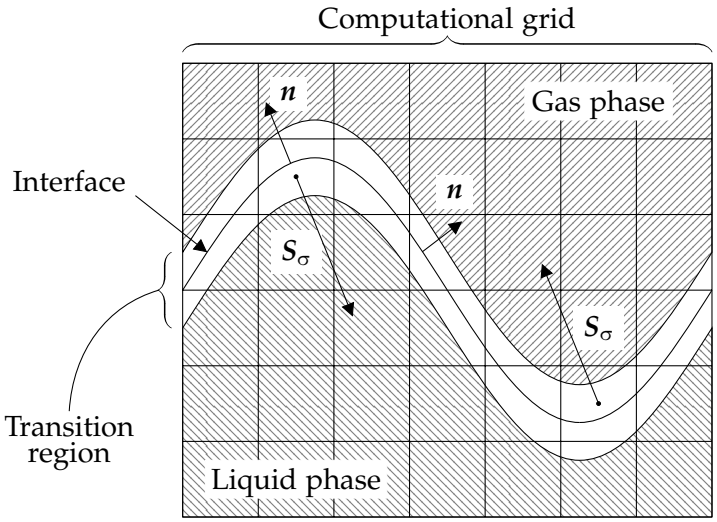

Figure 4.1: The figure shows the direction the surface tension force, $\boldsymbol{S}_\sigma = \sigma\kappa\nabla\alpha_c$, between the gas and liquid phases depending on the curvature of the interface (Brackbill et al. 1992).

In order to model interfacial turbulent flows, the interface between the phases must be captured as well. This is done by the VoF method, which is described in the next section. Furthermore, the unresolved SGS turbulence is modelled using the wall-adapting local eddy-viscosity model proposed by Franck and Ducros (1999). It accounts for the effects of both strain and rotation rate at the SGS scale while ensuring that the eddy viscosity tends to zero near the wall (McGinn et al. 2018).

4.2 Volume of Fluid Method

The VoF method is a computational fluid dynamics (CFD) technique used to simulate the behaviour of immiscible fluid interfaces, which was originally formulated by Hirt and Nichols (1981). It is based on the concept of tracking the volume fraction of each fluid phase within each computational cell to determine the interface between each phase.

In the VoF method the volume fraction of the liquid phase, α, is introduced with an additional transport equation as shown in Equation 4.5. The α value is bounded between 0 and 1 in any given cell (Gamet et al. 2020).

$$\frac{\partial \alpha}{\partial t} + \nabla \cdot (\alpha \overline{\boldsymbol{u}}) = 0 \tag{4.5}$$

$$\alpha = \begin{cases} 1 & \text{Occupied by liquid phase} \\ 0 & \text{Occupied by gas phase} \\ 0 < \alpha < 1 & \text{Occupied by a mixture of liquid and gas phase} \end{cases} \tag{4.6}$$

The interface between two fluid phases is represented by a sharp discontinuity in the volume fraction values. The piecewise linear interface construction method reconstructs the interface by a plane within each cell in the domain. An example is shown in Figure 4.2, where a two-dimensional interface is constructed based on the volume fraction in each cell.

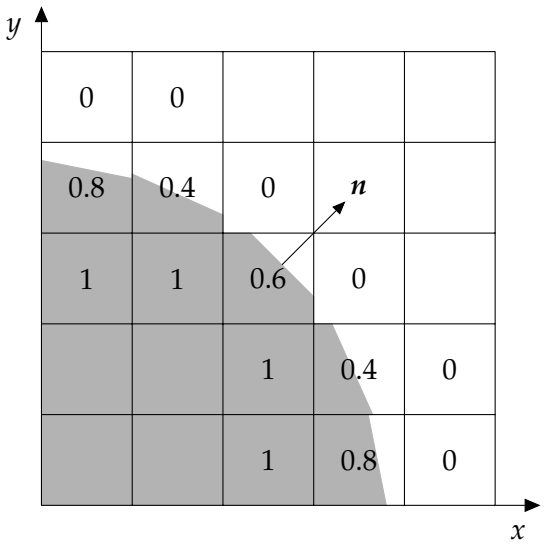

Figure 4.2: Schematic of the piecewise linear interface construction method for capturing the interface between the gas and liquid phase.

The plane is oriented according to the volume fraction gradients between the adjacent cells. The normal vector of the plane in each cell can then be computed based on these gradients as pre-

viously shown in Equation 4.4 (Karch et al. 2013). The plane can then be translated along the direction of the normal vector to ensure the volume enclosed by the cell boundaries and the plane is equal to the volume fraction at the cell centre, α_c.

The density and other material properties, such as viscosity, are calculated by volume averaging according to Equation 4.7, where the volume of the liquid phase is tracked.

$$\rho = \rho_l \alpha + \rho_g (1 - \alpha), \qquad \mu = \mu_l \alpha + \mu_g (1 - \alpha) \tag{4.7}$$

where the subscripts l and g refer to the liquid and gas phases. The interface between the phases needs to be reconstructed in each cell since information is lost when the interface is represented solely by the volume fraction.

4.3 Numerical Determination and Visualisation of Droplet Size

In this study, the droplet size is determined from the interphase between the gas and liquid. The volume fraction is used to split the domain into regions of separate phases based on a threshold value set to 0.5. The number of droplets traversing the outlet boundary patch is counted as a function of time. The volumes of non-spherical droplets and ligaments traversing the outlet boundary patch are converted into equivalent spheres and the resulting diameter is measured, as visualised in Figure 4.3.

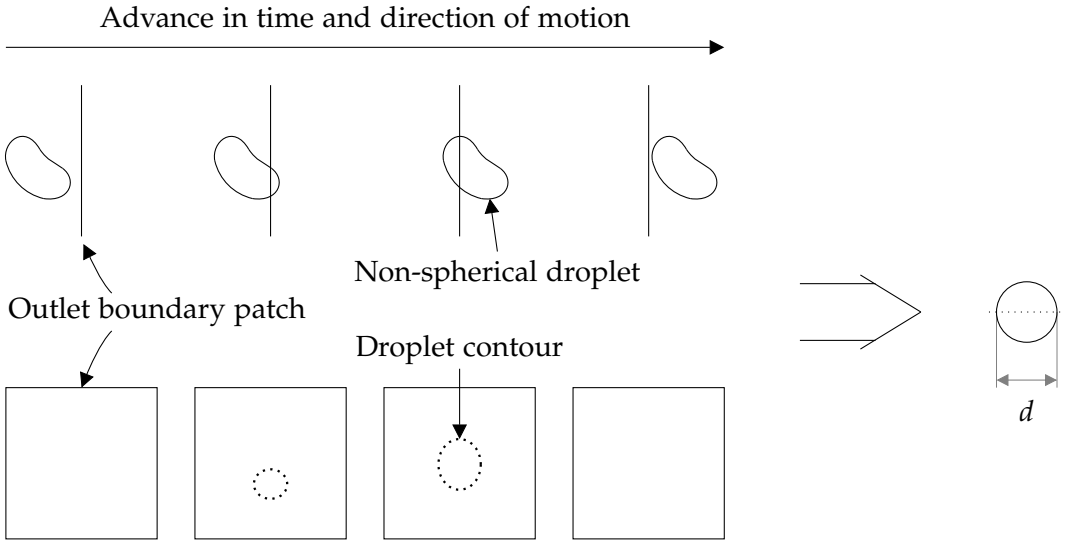

Figure 4.3: Visualisation of the conversion of non-spherical droplets and ligaments into equivalent spheres with diameter d after traversing the outlet boundary patch.

The droplets are then grouped based on diameter and plotted in a histogram. A probability

distribution is then fitted to the histogram data to reproduce the droplet size distributions. One of the most common distributions used in studies of atomization is the lognormal (Panão 2023). A lognormal distribution is applied based on the droplet distribution histogram according to Equation 4.8 to make a probability density function that describes the droplet size distribution (Kissell and Poserina 2017).

$$f_{\text{PDF}} = \frac{1}{\sigma N_d \sqrt{2\pi}} \exp\left(-\frac{(\ln(N_d) - \mu)^2}{2\sigma^2}\right) \tag{4.8}$$

where σ is the standard deviation, μ is the sample mean, and N_d is the number of droplets at a given diameter. An example of a lognormal distribution fit to a droplet distribution histogram is given in Figure 4.4.

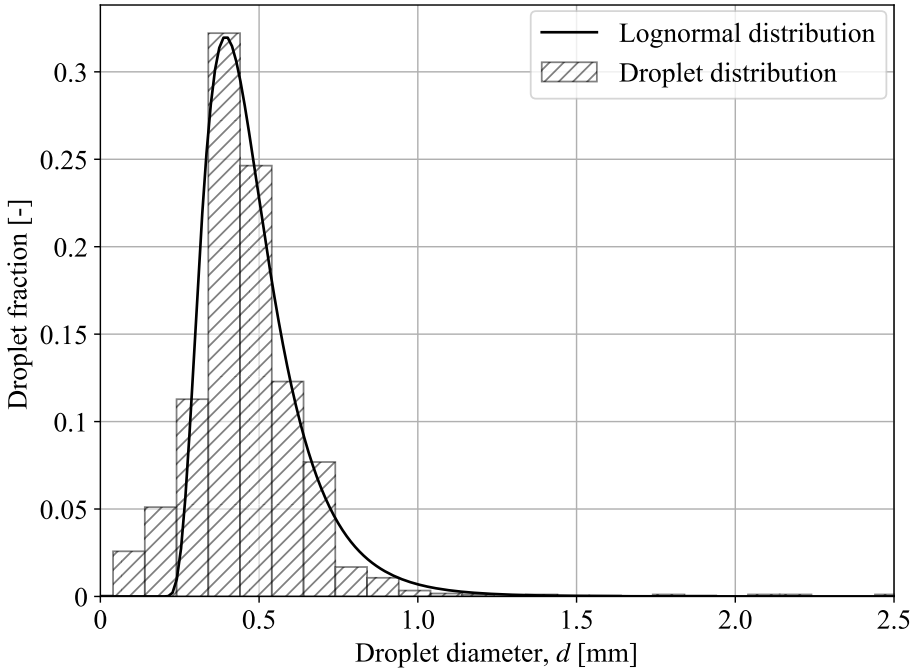

Figure 4.4: Lognormal distribution fit to the droplet distribution histogram.

4.4 Computational Domain and Boundary Conditions

Since droplet formation is of interest in this study, the computational domain consists of the investigated nozzle and an atmospheric cube downstream of the nozzle outlet. The dimensions of the investigated nozzle have previously been presented in Section 2.4 and the dimensions of the atmospheric cube can be seen in Figure 4.5, where D = 2.5 mm.

Two different distances downstream of the nozzle outlet have been investigated due to the missing information regarding the distance at which the droplet size measurements were obtained.

This revealed that the downstream distance of $8D$ produced the most accurate droplet size distribution compared to the experimental data. The comparison between the downstream distance of $8D$ and $15D$ is included in Appendix B on page 55. The computational domain seen in Figure 4.5 is therefore used as default throughout the rest of this study.

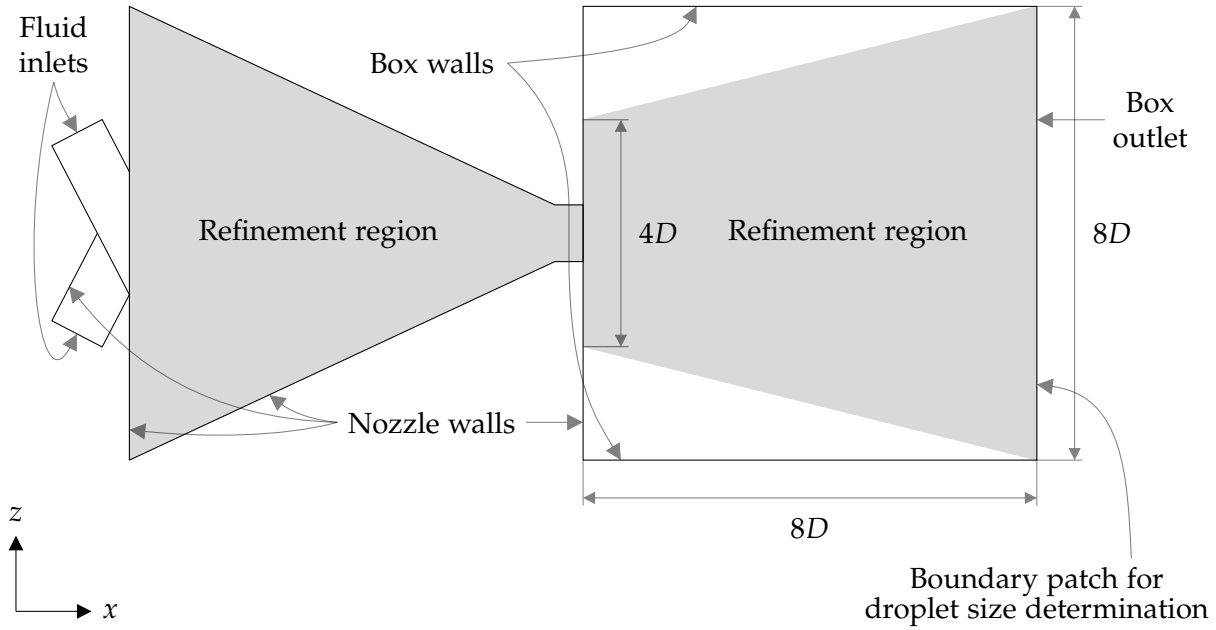

Figure 4.5: Schematic of the computational domain with dimensions given for the atmospheric cube and truncated refinement cone downstream of the nozzle as well as the imposed boundary conditions.

The computational domain needs to be supplied with boundary conditions to constrain the solution variable. To reflect the physical conditions of the experimental setup, the boundary conditions presented in Table 4.1 are implemented. Furthermore, the boundary conditions have also been marked in Figure 4.5. The contact angle of water on the nozzle walls has been set to 75 ° based on the findings by Bernardes et al. (2010) with water and stainless steel.

Table 4.1: Overview of the boundary conditions in the computational domain.

Boundary	$\boldsymbol{u}$	p	α
Gas inlet	Velocity profile	$\frac{\mathrm{d}p}{\mathrm{d}x} = 0$	Value of 0
Water inlet	Velocity profile	$\frac{\mathrm{d}p}{\mathrm{d}x} = 0$	Value of 1
Nozzle walls	No-slip condition	$\frac{\mathrm{d}p}{\mathrm{d}x} = 0$	Contact angle
Box outlet	Outlet	Atmospheric	Outlet
Box walls	Outlet	Atmospheric	Outlet

4.4.1 Inlet Fluid Velocity Profiles

As the inlet flow of the air and water is assumed to be fully developed, analytical expressions for the velocity profiles have been applied (Štigler 2012). For the turbulent water flow the velocity profile is approximated by the power law equation:

$$u = \frac{u_{\text{bulk}}}{2}\left(\frac{1}{n}+1\right)\left(\frac{1}{n}+2\right)\left(1-\frac{r}{R}\right)^{1/n} \tag{4.9}$$

where u_{bulk} is the average bulk velocity the inlet, R is the radius of the pipe and r is the local radial distance. n is a coefficient that is a function of the Reynolds number and has to be determined experimentally. However, a value of 7 is reasonable for many practical flow approximations (Štigler 2012). For the laminar gas flow, the velocity profile is given by:

$$u = 2u_{\text{bulk}}\left(1-\left(\frac{r}{R}\right)^2\right) \tag{4.10}$$

The two corresponding velocity profiles are presented in Figure 4.6.

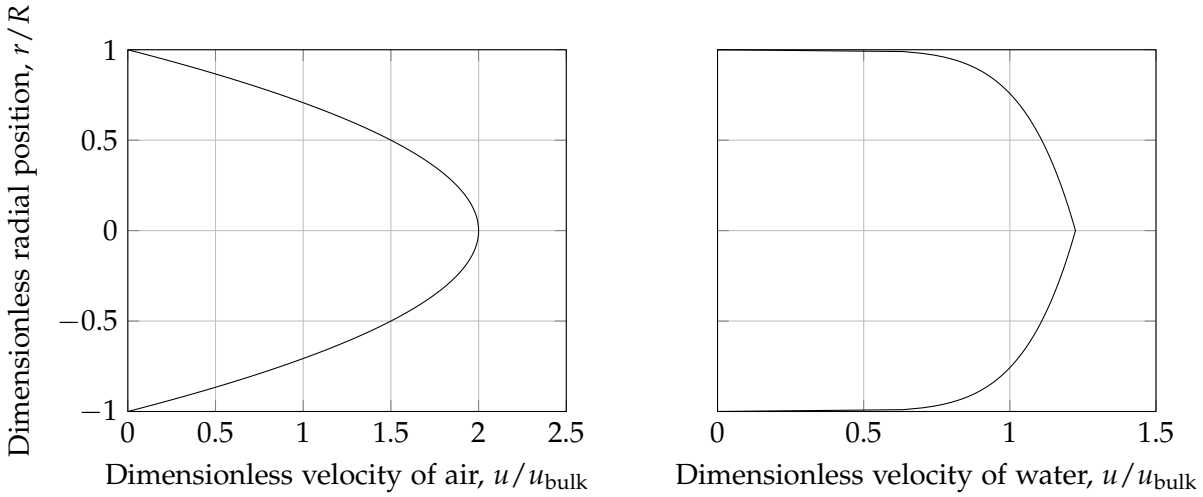

Figure 4.6: Dimensionless inlet velocity profiles of air and water.

4.5 Mesh Topology

In Figure 4.7a, a slice of the full mesh consisting of 3,195,984 cells is presented in the x-y plane. Two mesh refinement regions have been included in central areas of turbulent mixing and atomization. These refinement regions have also been included in Figure 4.5. A fine mesh is needed in these areas to properly capture the interface between the gas and liquid phases inside the nozzle chamber dominated by turbulent mixing and downstream of the nozzle orifice where the droplets are formed. The refinement region downstream of the nozzle is a truncated cone. The

minor diameter of $4D$ seen in Figure 4.5 ensures the spray angle is properly captured and the droplets do not cross the transition between refinement regions. The height of the first cell layer is kept to a value of $3{\cdot}10^{-3}$ m to achieve a y^+ value of approximately 1. However, due to the high velocity in the nozzle throat, values of 2 to 3 were reached during the simulations.

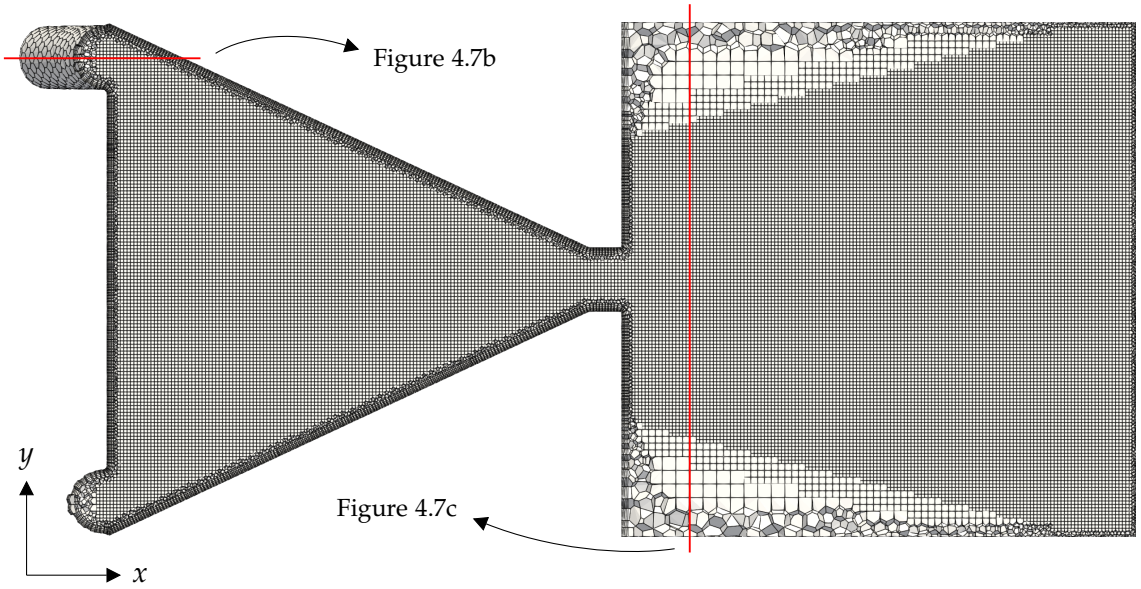

(a) Slice of the full mesh in the x-y plane.

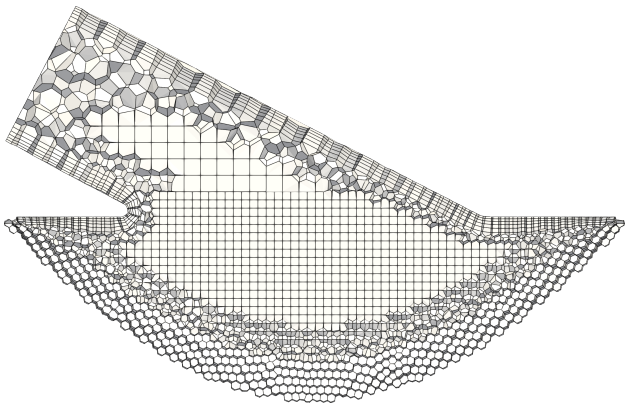

(b) Visualisation of the inlet pipe in the fine mesh showcasing the rounded corner due to the imposed fillet.

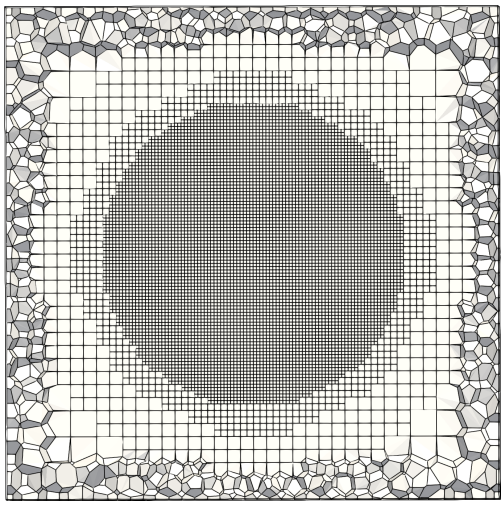

(c) Cross-sectional view of the mesh at a distance of $1D$ downstream of the nozzle orifice.

Figure 4.7: Overview of the fine mesh used in the simulations.

In Figure 4.7c, a cross-sectional view of the mesh is presented at a distance of $1D$ downstream of the nozzle orifice showcasing the circular refinement region in the middle of the downstream domain. Figure 4.7b presents a slice down the middle of one of the inlet pipes. Furthermore,

fillets have been added to locations in the nozzle geometry where acute angles complicate the meshing process. This is visible in Figure 4.7b as better mesh quality is achieved where the inlet pipe is attached to the nozzle. In Figure 4.8, a zoom-in of the nozzle inlet section is presented where the exact placement and dimension of the fillets have been included. Lastly, polyhedral cells have been used in the mesh due to the conical nozzle shape and inclined inlet pipes.

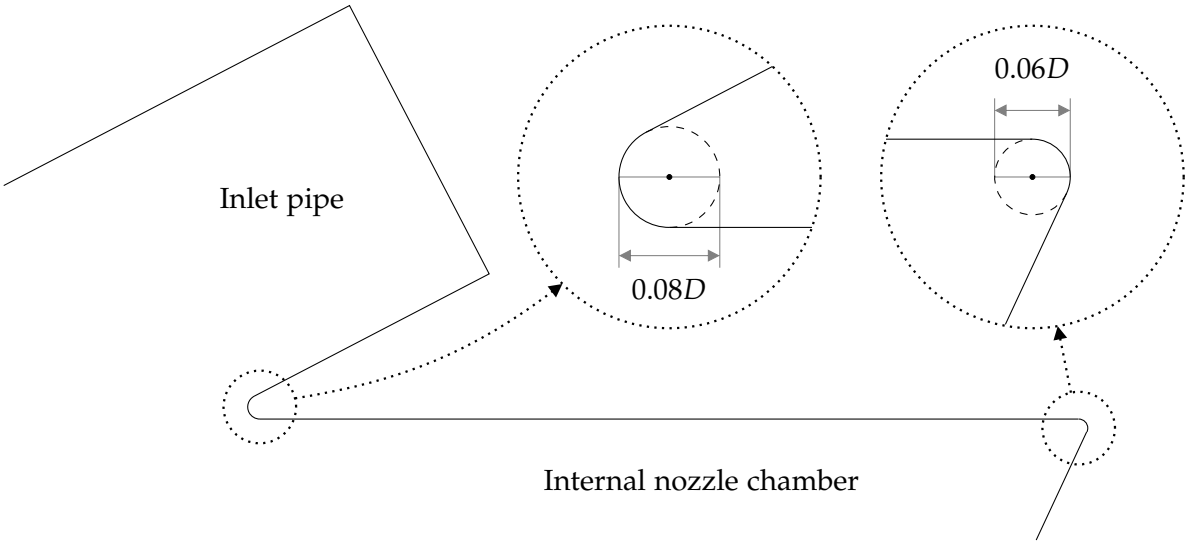

Figure 4.8: Schematic of the nozzle inlet section with the added fillets and their dimensions.

4.6 Initialisation Process

In this study, simulations have been initialised with a flow field to reduce computational time. The flow field used for initialisation is visualised in Figure 4.9c where the air has been replenished 51 times in the nozzle. During the initialisation process, a slightly conical air core gradually forms within the nozzle due to the conical nozzle shape and inclined inlet pipes. The internal flow of the swirl nozzle is consistent with the theory described in Chapter 3 on page 11, where an air core forms in the centre of a single-fluid swirl nozzle. However, there is a slight difference as a twin-fluid swirl nozzle is investigated in this study.

Figure 4.9 depicts the evolution of the time-averaged isosurface. The isosurface represents the interface between the gas and liquid phases within the swirl nozzle. A volume fraction value of 0.5 is chosen to visualise the interface, where the air is contained within the isosurface and water surrounds it. Furthermore, the volume inside the stabilised isosurface presented in Figure 4.9c is used to calculate the normalised time, t^*. As the isosurfaces depicted in Figure 4.9a and 4.9b both contain larger volumes of air, the calculated normalised time will therefore be slightly misleading in terms of the number of times the air inside the nozzle has been replenished.

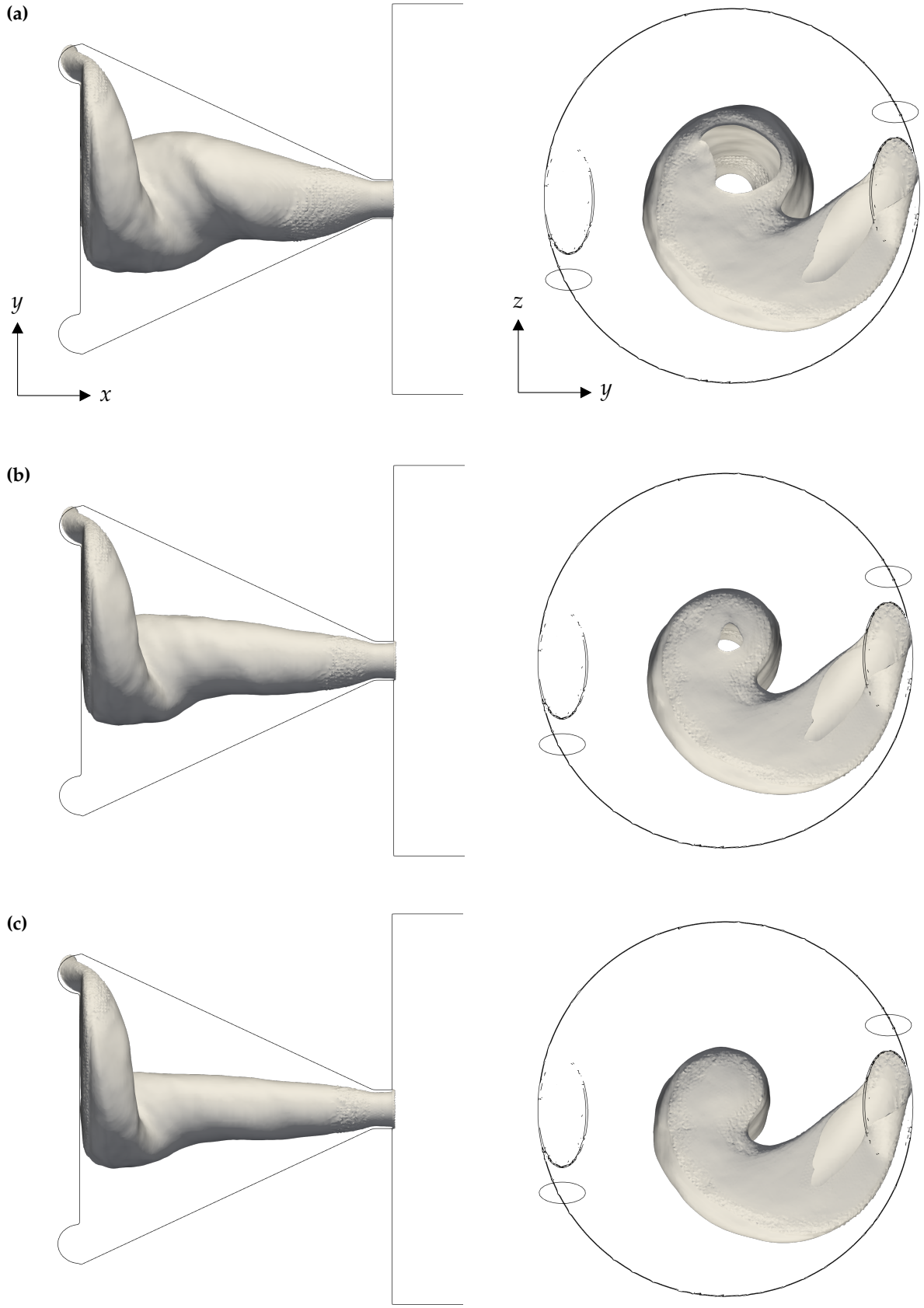

Figure 4.9: The figures show the time-averaged isosurface of the interface between the water and air phases at: **(a)** $t^* \approx 31.9$, **(b)** $t^* \approx 41.4$, and **(c)** $t^* = 51$. A water volume fraction of 0.5 is used to represent the isosurface.

5 Verification and Validation

In this chapter, the numerical model will first be verified through a time and grid independence study. The time independence study is conducted to ensure the results are independent of the sample time. Secondly, the results of the numerical model will be validated with the experimental data from the study by Ochowiak (2016).

5.1 Time Independence Study

The time-averaged data results should not change significantly over time to ensure the simulations are reliable. The change in velocity and droplet size is therefore investigated as functions of time in this section. The magnitude of the instantaneous and mean velocities are sampled at different axial positions throughout the computational domain. The required simulation time to achieve a reliable averaging period can then be determined. The sampling locations are visualised in Figure 5.1.

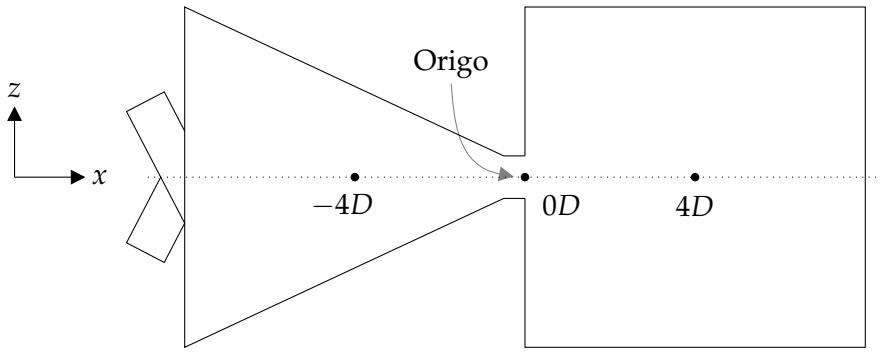

Figure 5.1: Schematic of the computational domain with the three locations marked where the instantaneous and mean velocities have been sampled.

The instantaneous data points are written every 0.1 ms, while the mean data represents the mean over every simulated time step. It can be seen that at $t^* = 4$, which indicates that the air inside the nozzle has been replenished four times, the mean profiles flatten and remain fairly stable. Therefore, a simulation time of $t^* = 16$ is assumed to be sufficient to obtain accurate mean data.

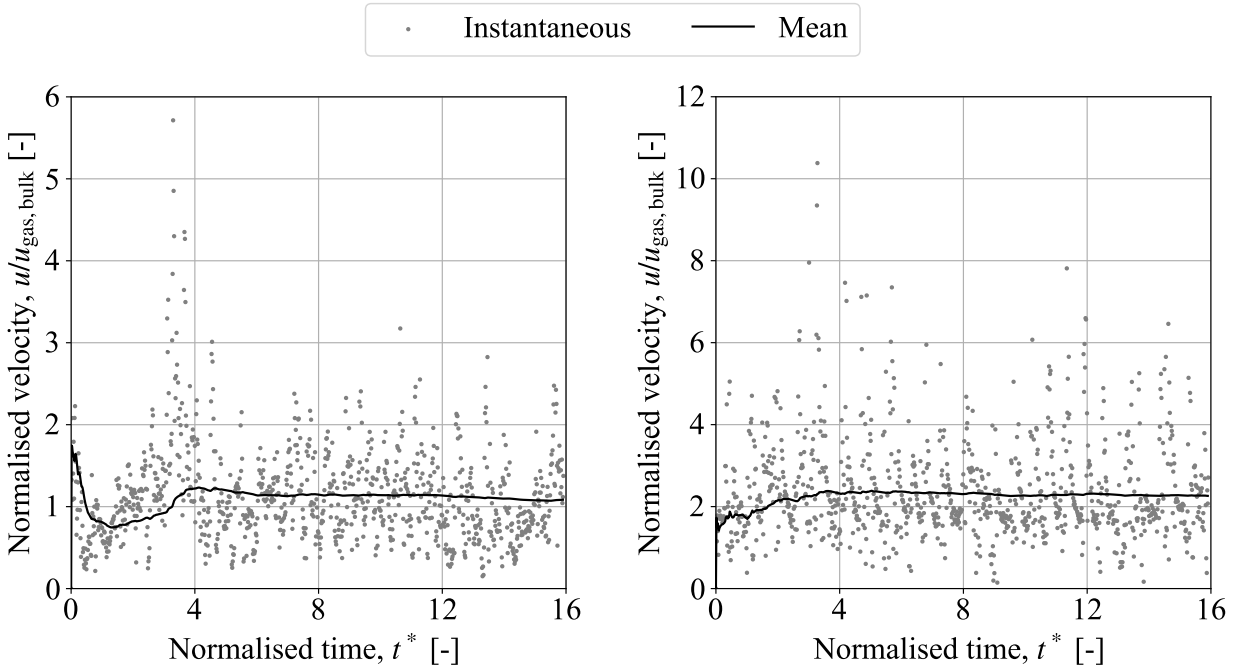

(a) Sampled velocity at $x/D = -4$.

(b) Sampled velocity at $x/D = 0$.

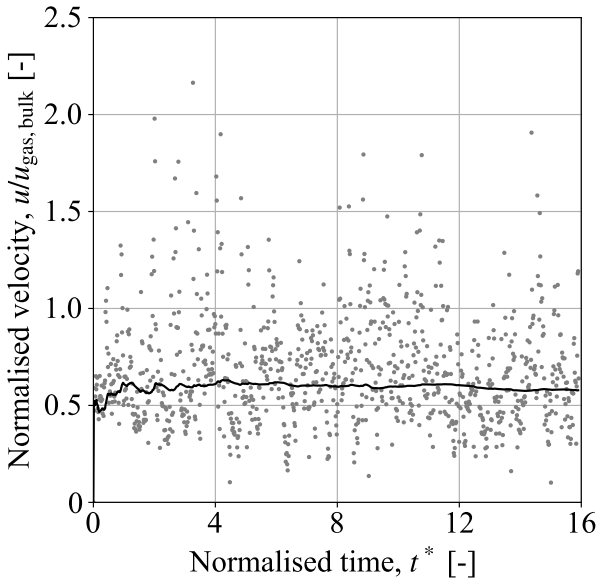

(c) Sampled velocity at $x/D = 4$.

Figure 5.2: The figures show the sampled instantaneous and mean velocity magnitude at different axial positions throughout the computational domain as a function of the normalised time, $t^* = \left(\dot{Q}_{\text{air,bulk}}/V_{\text{air}}\right) t$.

The change in the arithmetic mean droplet diameter, D_{10}, and Sauter mean diameter (SMD), D_{32}, is also measured as a function of time to see if the simulated values remain stable. The SMD considers both the number of droplets and their respective volumes, thus providing a more comprehensive representation of the droplet size distribution. It is calculated based on Equation 5.1:

$$D_{32} = \frac{\sum_{i=1}^{n} d_{\text{i}}^3 \cdot N_{\text{d,i}}}{\sum_{i=1}^{n} d_{\text{i}}^2 \cdot N_{\text{d,i}}} \tag{5.1}$$

where $N_{d,i}$ and d_i are the number and diameter of the droplets respectively. Since larger droplets contribute more to the overall volume of the droplets, SMD is weighted towards the larger droplets. This means that the SMD is more sensitive to changes in the size of larger droplets compared to smaller ones. Unlike the arithmetic and volume mean diameter, which focus solely on the number and volume fractions respectively, the SMD balances both.

In this case, the simulated droplets were collected over intervals of 0.02 seconds which corresponds to $t^* = 3.186$. Therefore, the D_{10} and D_{32} represent the respective average droplet diameters that were collected between each marker. The mean of the markers is represented by the solid and dashed lines. It is evident that both methods of averaging the droplet size remain stable over time, which indicates the simulation time of $t^* = 16$ is assumed to be sufficient to obtain accurate mean data of the droplet size distribution.

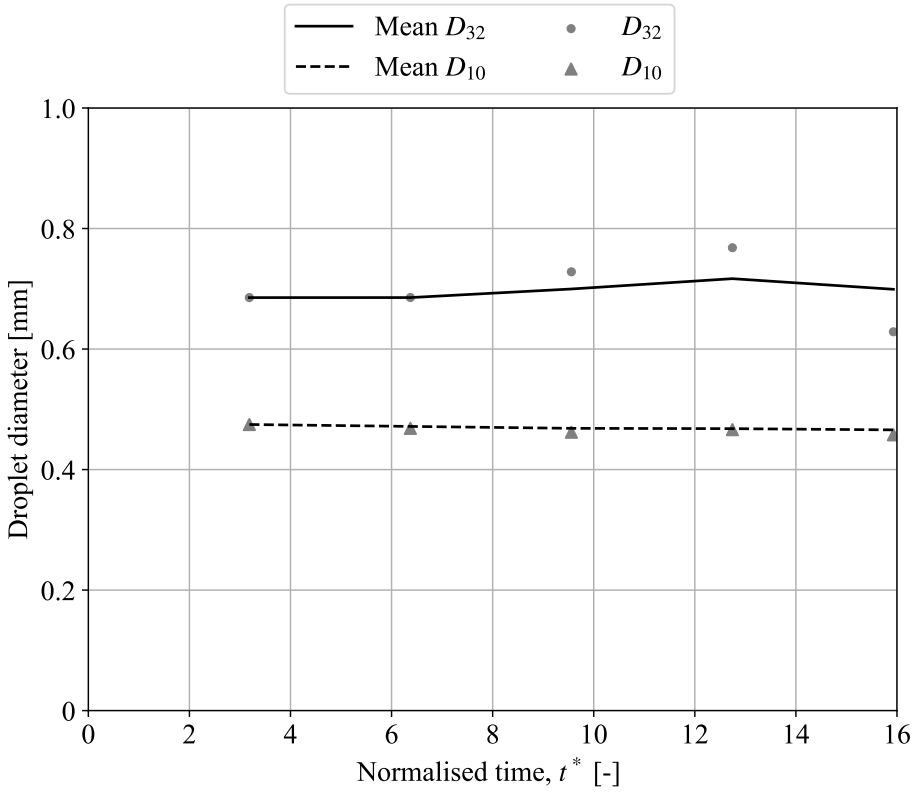

Figure 5.3: The figure shows the change in droplet size as a function of the normalised time, $t^* = \left(\dot{Q}_{\text{air,bulk}}/V_{\text{air}}\right) t$, using the arithmetic mean droplet diameter, D_{10}, and Sauter mean diameter, D_{32}.

5.2 Grid Independence Study

To ensure the results are independent of mesh refinement, a grid independence study is conducted. The variable of interest is the mean droplet diameter, which is measured on the outlet boundary patch over a duration of 0.1 seconds. The study is based on three different mesh sizes, a coarse mesh with 795,935 cells, a medium mesh with 1,590,604 cells, and a fine mesh with 3,195,984 cells. The droplet size data is visualised with a probability density function (PDF) based on a lognormal distribution as seen in Figure 5.4 for the three mesh sizes.

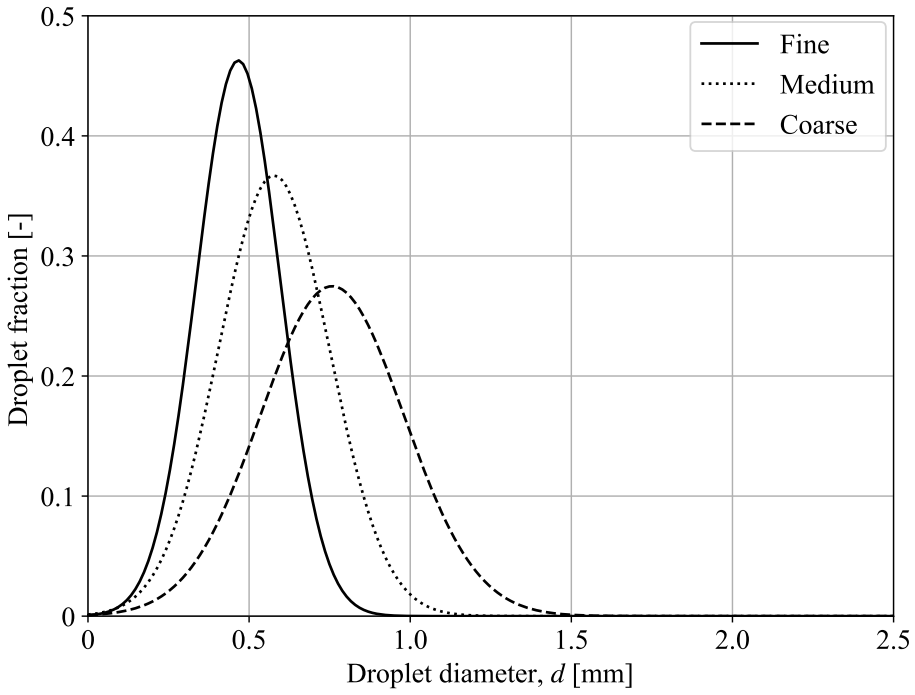

Figure 5.4: Lognormal distribution of the three mesh refinement levels.

It is evident that lower mesh refinement results in larger droplets and a PDF shifted to the right. The opposite is seen for the fine mesh, which captures a larger portion of the small droplets. The lognormal distribution and the mean diameter given in Table 5.1 show a smaller difference between the medium and fine mesh compared with the coarse and medium mesh. Additionally, the shape of the lognormal distribution is mostly similar between the medium and fine meshes.

The difference in the droplet size distribution between the different mesh refinement levels can be attributed to how droplets are represented in the VoF method, where the mesh refinement greatly influences the sharp interface between the two phases. An increase in refinement level will increase the number of smaller droplets, as one droplet in the coarse mesh might be two or more droplets lying close together in the fine mesh. This could explain the sharp peak in the smaller droplets for the fine mesh, while the fraction of larger droplets decreases.

Table 5.1: Comparison of mean diameter for the different mesh sizes.

	Mean diameter [mm]
Coarse	0.753
Medium	0.559
Fine	0.466

In order to further verify the mesh independence of the simulations, a grid convergence index (GCI) is calculated based on the approach proposed by Roache (1994). In this approach, the analysis is performed on three data points, f_1, f_2 and f_3 obtained at a different number of computational cells, $N_{\text{cells},1}$, $N_{\text{cells},2}$ and $N_{\text{cells},3}$. The subscripts 1, 2, and 3 denote the fine, medium, and coarse mesh respectively. The three data points represent the mean diameter measured in each of the simulations. The order of convergence, O, is defined by:

$$O = \frac{\ln\left(\frac{f_3 - f_2}{f_2 - f_1}\right)}{\ln(\gamma)} \tag{5.2}$$

where γ is the grid refinement ratio with a value of approximately 2. Using the three simulated data points, a Richardson extrapolation can be used to find the ideal value, f_0, corresponding to a grid spacing of zero.

$$f_0 \cong f_1 + \frac{f_1 - f_2}{\gamma^{\mathrm{O}} - 1} \tag{5.3}$$

The GCI is calculated to give a percentile error between the ideal value and the simulated data points.

$$GCI = \frac{F_{\mathrm{s}}|\epsilon|}{\gamma^{\mathrm{O}} - 1}, \qquad \epsilon = \frac{f_2 - f_1}{f_1} \tag{5.4}$$

where the safety factor, $F_{\mathrm{s}} = 1.25$, is used for comparison of three or more meshes. Using this safety factor, error bands can be set according to Equation 5.5 for the extrapolated value based on the GCI.

$$f_0^+ = f_0 \cdot (1 + GCI), \qquad f_0^- = f_0 \cdot (1 - GCI) \tag{5.5}$$

The results can be seen in Figure 5.5. The fine mesh with 3,195,984 cells is within the limits of the safety factor. This further supports that the fine mesh will provide sufficiently mesh-independent results. The fine mesh is presented in Figure 4.7.

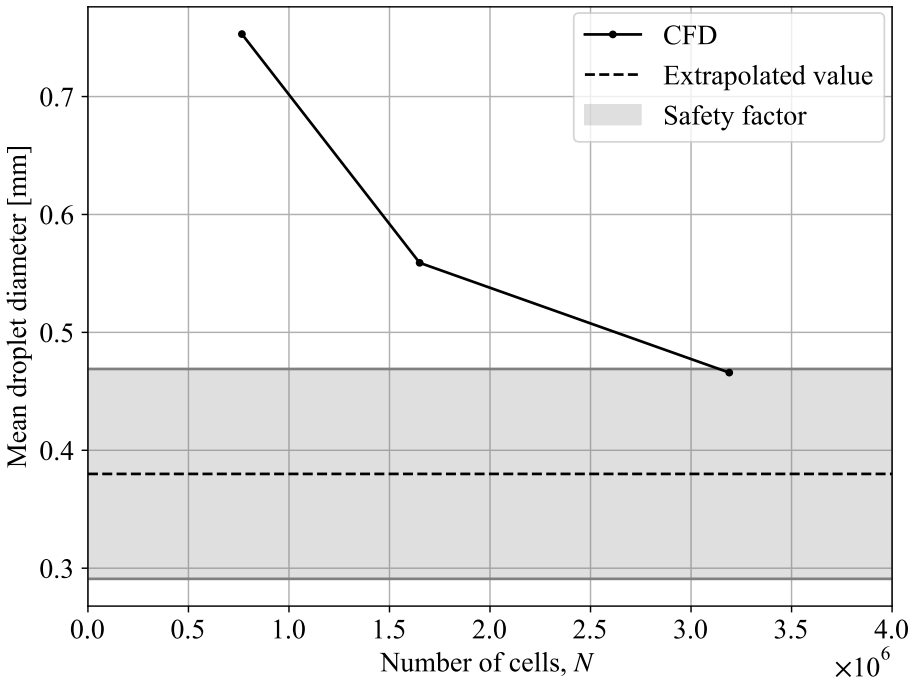

Figure 5.5: Grid convergence index analysis of the three refinement levels.

Several parameters can be used to evaluate the quality of a mesh. These parameters include the cell aspect ratio which is defined as the ratio of the longest edge length to that of the shortest edge length within a cell. This is illustrated in Figure 5.6, where the cell aspect ratio increases from 1 to 2, due to the length of the cell, δ_L. Ideally, the cell aspect ratio should be one, but values below five are generally accepted. In the boundary layer, aspect ratios of 10 to 20 are generally accepted (ANSYS 2009). The skewness of a cell describes the deformation of a cell. It is defined by the deviation between the vector that connects two cell centres and the face centre. The concept of non-orthogonality is visualised in Figure 5.6 with two adjacent cells and the shared cell face between them. The angle, θ, between the normal vector and the vector connecting the two adjacent cell centres determines the non-orthogonality value. This angle should generally be below 65 °(ANSYS 2009).

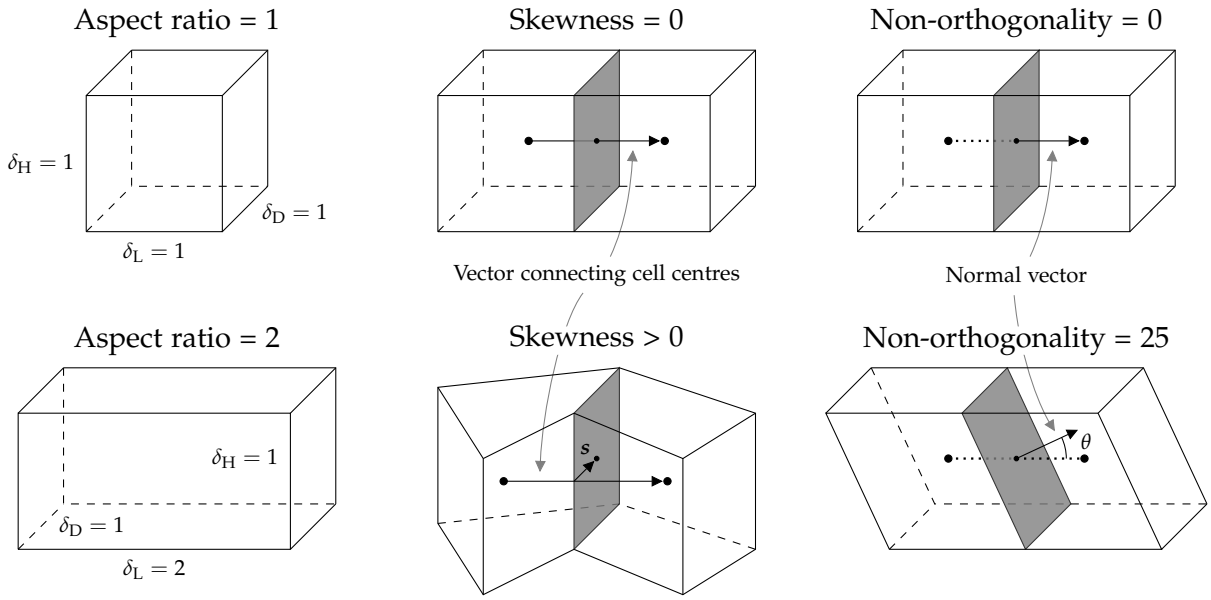

Figure 5.6: Visualisation of aspect ratio, skewness, and non-orthogonality.

Figure 5.7 shows the histograms of the aspect ratio, skewness, and non-orthogonality of the cells in the fine mesh. The mesh statistics of the coarse and medium mesh can be found in Appendix C on page 57. The fine mesh generally meets the mesh requirements. The high aspect ratios in the fine mesh are caused by the larger cells in the unrefined region immediately downstream of the nozzle orifice. Since these cells are located outside of the region of interest, the influence of the high aspect ratios on the results is deemed negligible.

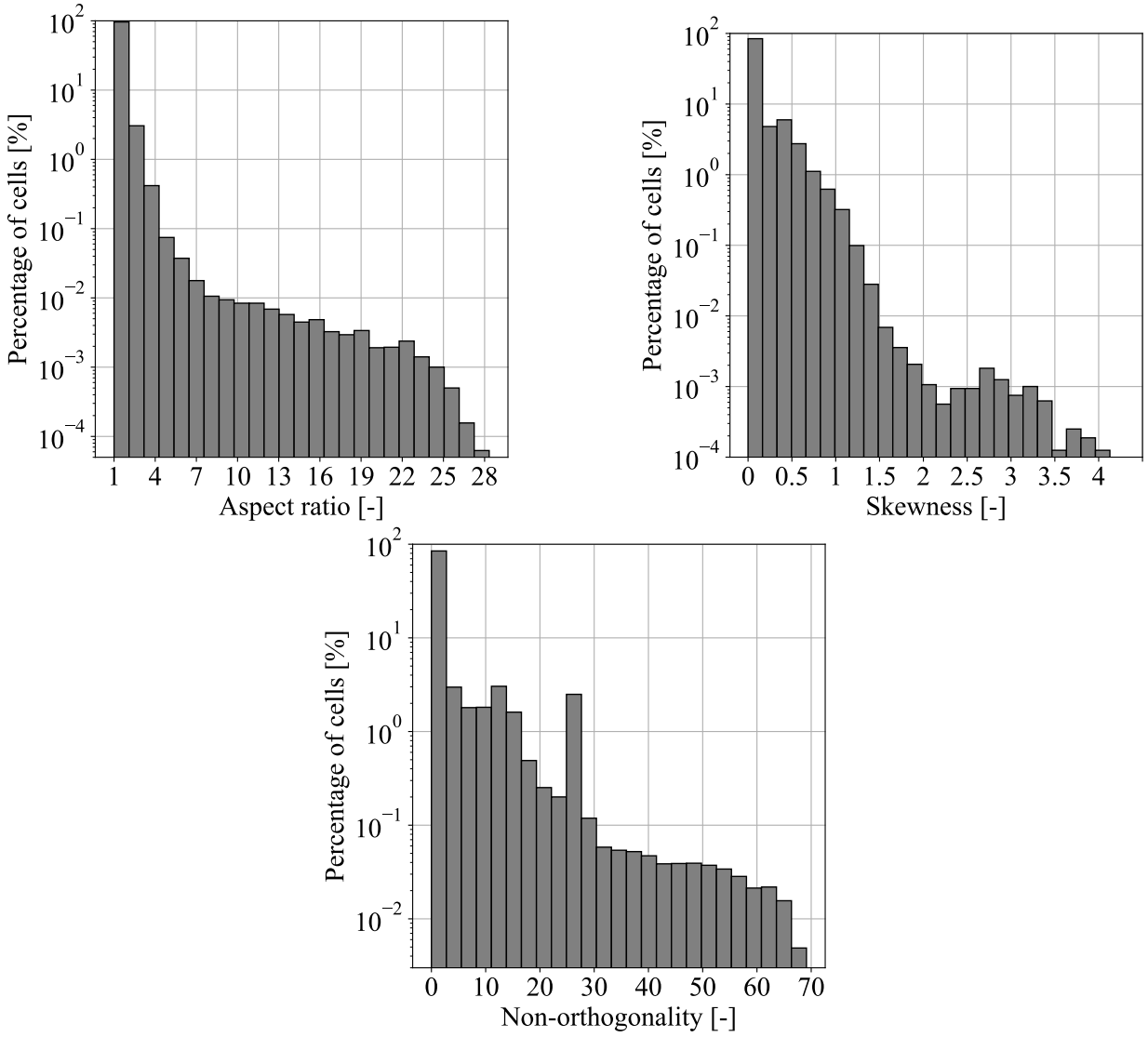

Figure 5.7: The figures show the percentage of cells in the fine mesh with a given cell aspect ratio, skewness, and non-orthogonality.

5.3 Visualisation of Volume Fraction and Velocity Flow Fields

Figures 5.8 and 5.9 present a snapshot of the simulated volume fraction and velocity field. The data fields are visualised by a slice in the x-y plane of the computational domain. In Figure 5.8 the instantaneous and time-averaged volume fraction field is presented. The breakup process is visible from the instantaneous flow field, where droplets and ligaments are seen to detach from the liquid core. As the conical liquid sheet spreads outwards, it becomes thin and eventually breaks into small droplets. Both turbulent structures and a wavy interface are visible inside the nozzle. This is caused by the shear stress between the gas and liquid due to the difference in velocities. On the outside of the nozzle wall, water is seen to accumulate as it sticks to the nozzle wall. However, this is not believed to affect the simulation results.

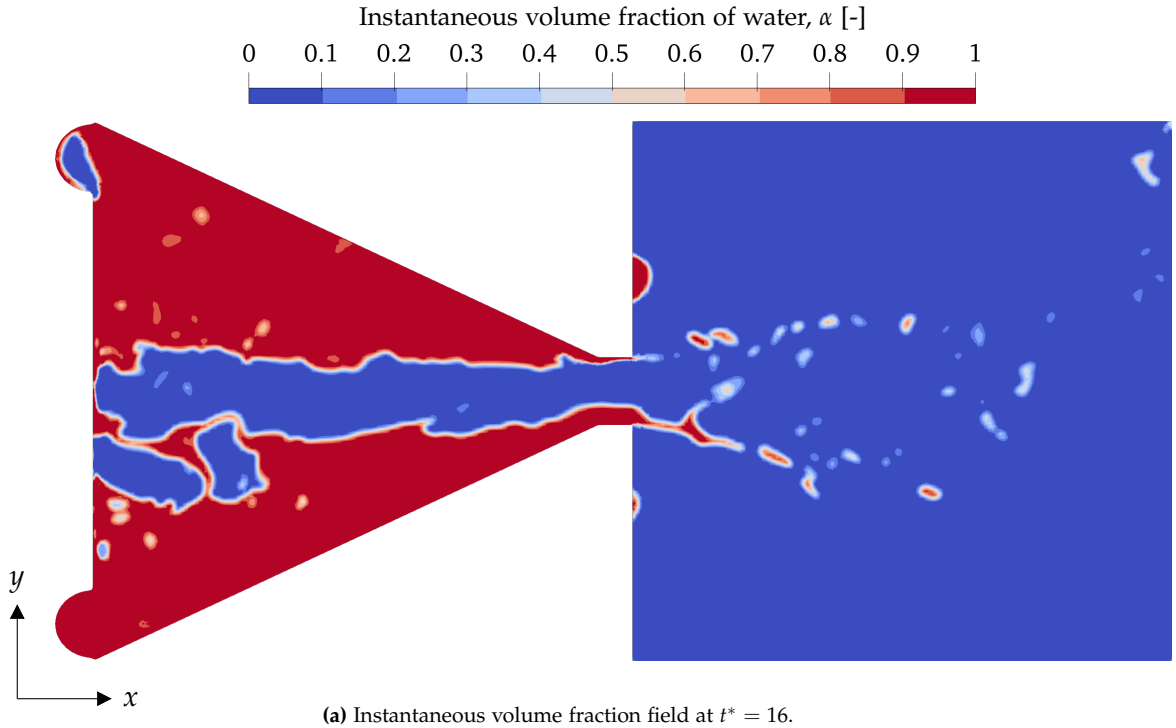

(a) Instantaneous volume fraction field at $t^* = 16$.

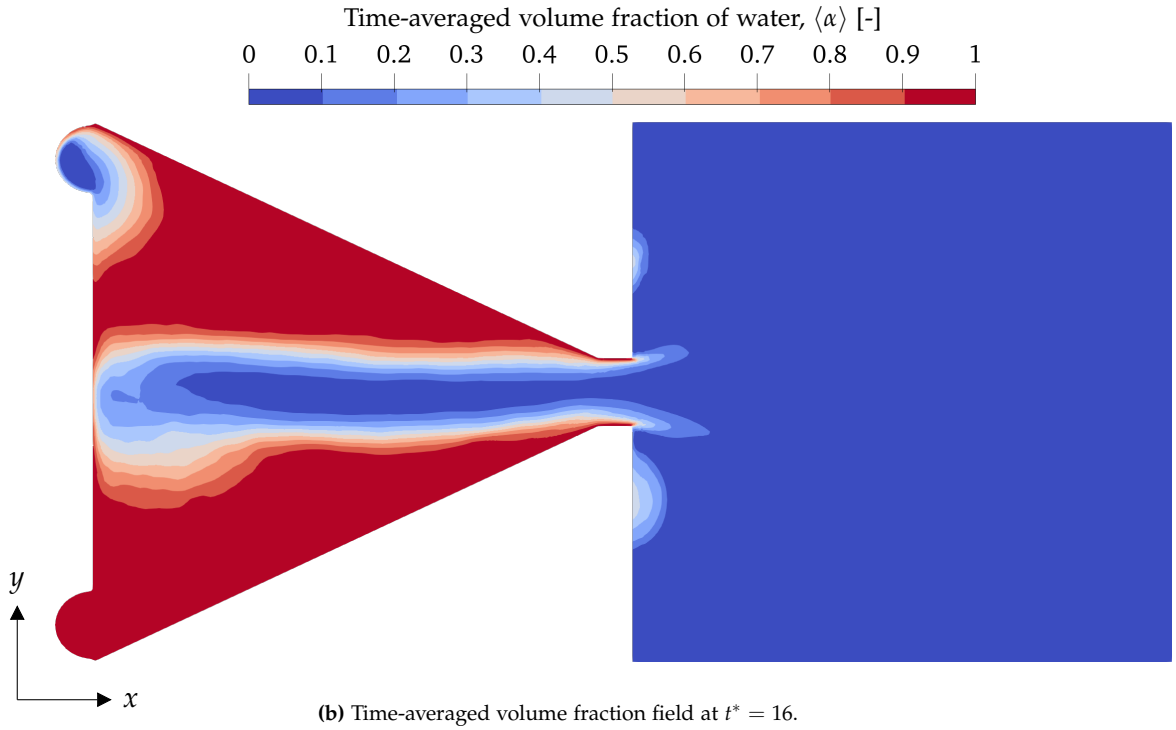

(b) Time-averaged volume fraction field at $t^* = 16$.

Figure 5.8: The figures show the instantaneous and time-averaged volume fraction fields throughout the computational domain at $t^* = 16$.

In Figure 5.9, the magnitude of the instantaneous and mean velocity field in the computational domain is presented. The highest velocities are located in the nozzle orifice and at the gas inlet pipe due to the liquid constricting the gas flow as it enters the nozzle.

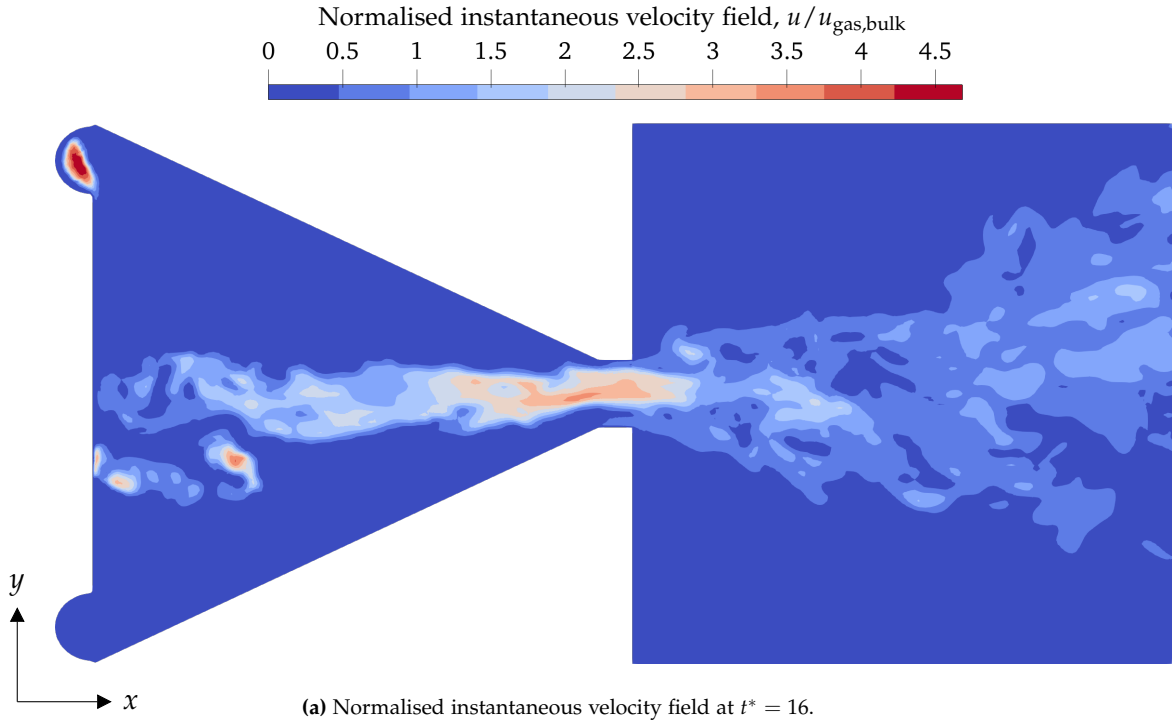

(a) Normalised instantaneous velocity field at $t^* = 16$.

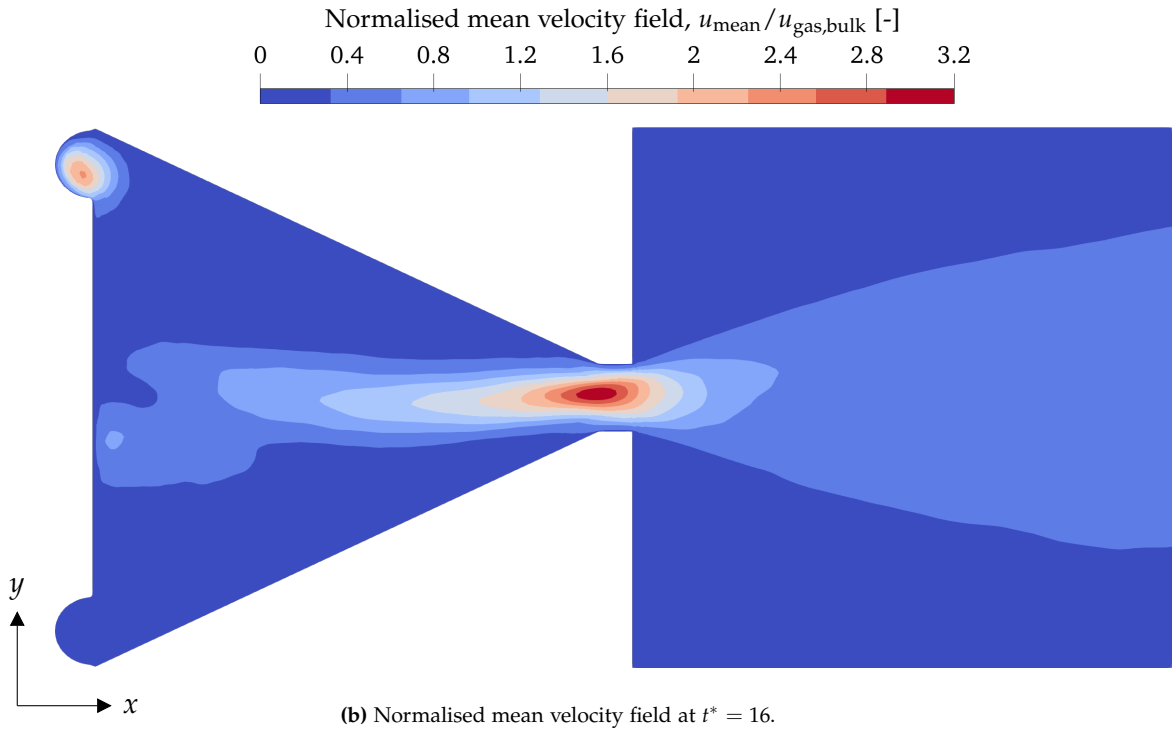

(b) Normalised mean velocity field at $t^* = 16$.

Figure 5.9: The figures show the normalised instantaneous and time-averaged velocity fields throughout the computational domain at $t^* = 16$.

5.4 Validation of CFD Simulations by Experiment

The following section presents the validation of the proposed numerical model in this project. The simulation results will be compared to experimental data for droplet size distribution. Firstly, the experimental setup used in the study by Ochowiak (2016) will be presented.

The experimental data originates from the study by Ochowiak (2016), which used reverse-lens microphotography to capture the droplet size during the experiments. Reverse-lens microphotography is a technique used to capture highly magnified images of small objects, such as water droplets. A regular camera lens is mounted in reverse onto the camera body, as this results in increased magnification of the droplets compared to the normal camera configuration (Ochowiak et al. 2014). Computer software is then used to find and study the droplet size from the highly magnified images. Figure 5.10 shows an overview of the experimental setup used in the study by Ochowiak (2016). The study investigated the design of an internal mixing twin-fluid swirl nozzle, where a swirling motion was generated due to the inclined inlet pipes.

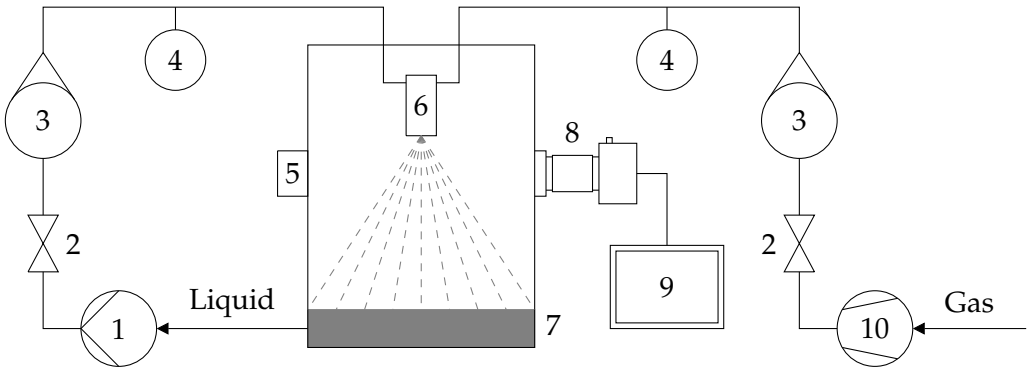

Figure 5.10: The experimental setup used in the study by Ochowiak 2016 is visualised. The components in the system are: 1. pump, 2. valves, 3. rotameters, 4. pressure gauges, 5. strobe, 6. atomizer, 7. tank, 8. camera, 9. computer, and 10. compressor.

The calculated SMD for each mesh size can be seen in Table 5.2. It is evident that the fine mesh is closer to the experimental SMD compared to the coarse and medium mesh. However, the PDF of the fine mesh is skewed compared to the experimental data seen in Figure 5.11, whereas the coarse and medium meshes are more accurate. However, the coarse and medium mesh are not mesh independent which may result in numerically inaccurate solutions. The fine mesh is therefore used throughout the rest of the study due to the mesh independence and the most accurate SMD of the three meshes investigated.

Table 5.2: Comparison of the Sauter mean diameter between the CFD simulations and experimental data.

	Sauter mean diameter [mm]	**Deviation from exp. [%]**
Coarse	1.045	24.4
Medium	0.67	20.2
Fine	0.698	16.9
Exp.	0.84	

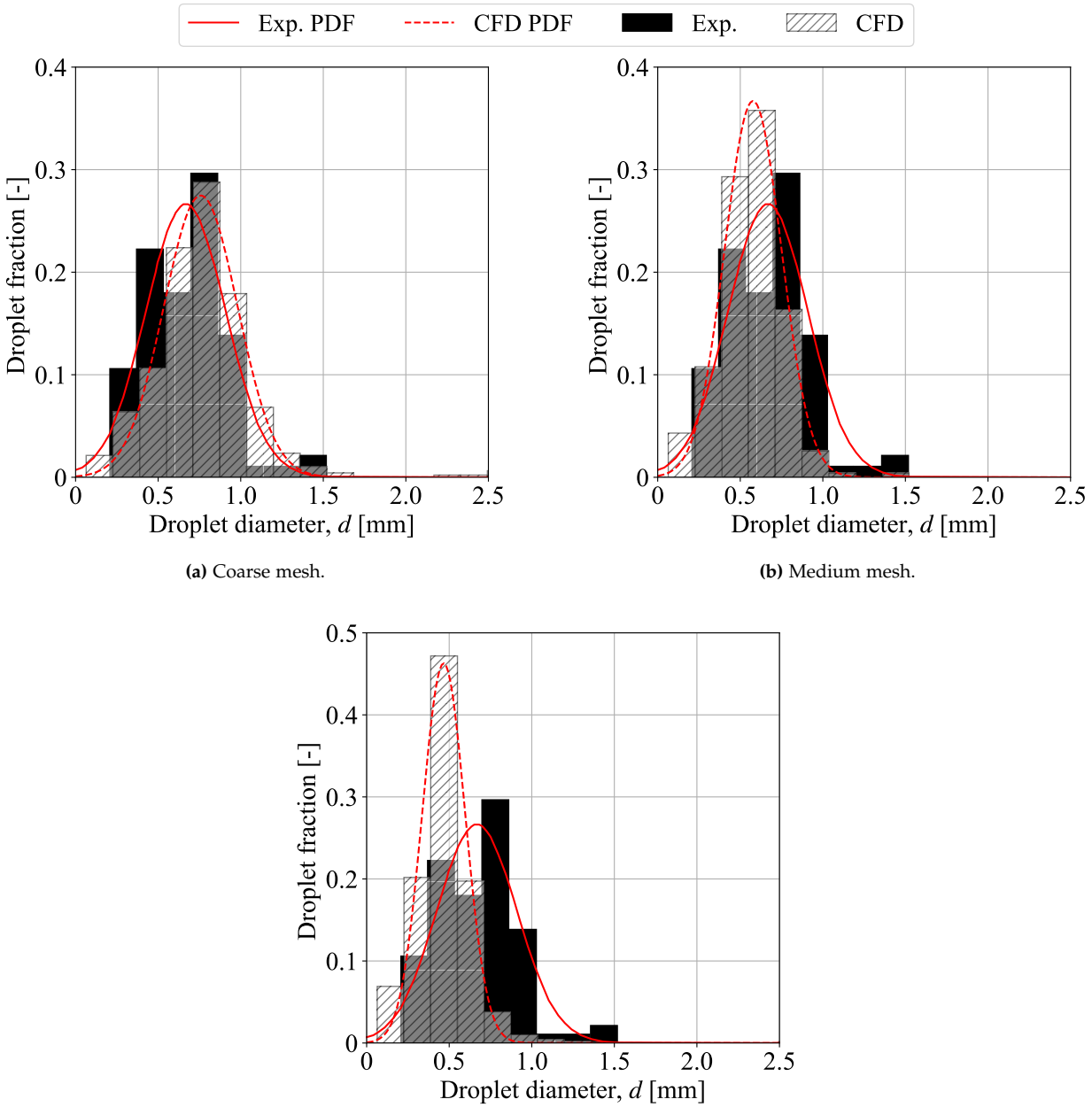

(a) Coarse mesh.

(b) Medium mesh.

(c) Fine mesh.

Figure 5.11: The figures show the droplet size distribution of the different mesh sizes compared to the experimental data.

6 Results and Discussion

In this chapter, a parametric study is conducted to examine the effect of varying the gas-to-liquid mass flow ratio (GLR) and inclination angle of the inlet pipes on the droplet size distribution. Furthermore, the symmetry and homogeneity of the spray downstream of the swirl nozzle will also be investigated.

6.1 Varying Gas-to-Liquid Mass Flow Ratio

The gas-to-liquid mass flow ratio (GLR) is an important parameter to investigate, as changes in the GLR can significantly influence the Sauter mean diameter (SMD). Higher GLRs typically result in smaller droplets due to increased atomization energy and breakup intensity. Three GLRs are investigated and compared in this section taking offset in the GLR used in the validation cases in the previous chapter, which was $6.85 \cdot 10^{-3}$. The additional two GLRs investigated correspond to 10 and 20 % increase in the GLR used in the validation case.

The gas phase transitions from laminar to turbulent flow due to the increase in GLR as shown by the increase in Reynolds number in Table 6.1. The reynolds number is higher than the critical Reynolds number for pipe flow of 2300. To account for the turbulent flow effect, the fixed velocity profile of the gas phase is changed from laminar to turbulent based on the equations previously presented in Section 4.4 on page 20.

Table 6.1: Operating conditions for the different GLRs investigated in the section.

GLR [-]	**Increase [%]**	**Re [-]**	
		Air	**Water**
0.00685	0	1980	5650
0.00754	10	2180	5650
0.00823	20	2379	5650

The results of the simulations are shown in Figure 6.1. The SMD decreases with an increase in GLR, which is consistent with the findings in the literature. The results show a fairly linear decrease in SMD with each incremental increase in GLR. This linear tendency might be attributed to the rather small increase in GLR of 10 and 20 % compared to the validation case. However, larger increments were not feasible given the increase in computational cost due to the higher velocities. Furthermore, the flow is assumed to be incompressible, and higher velocities could

result in the flow approaching compressible conditions. It is still clear that the increase in GLR results in a decrease in SMD. However, an increase in GLr of 20 % results in a 2.8 % decrease in the SMD.

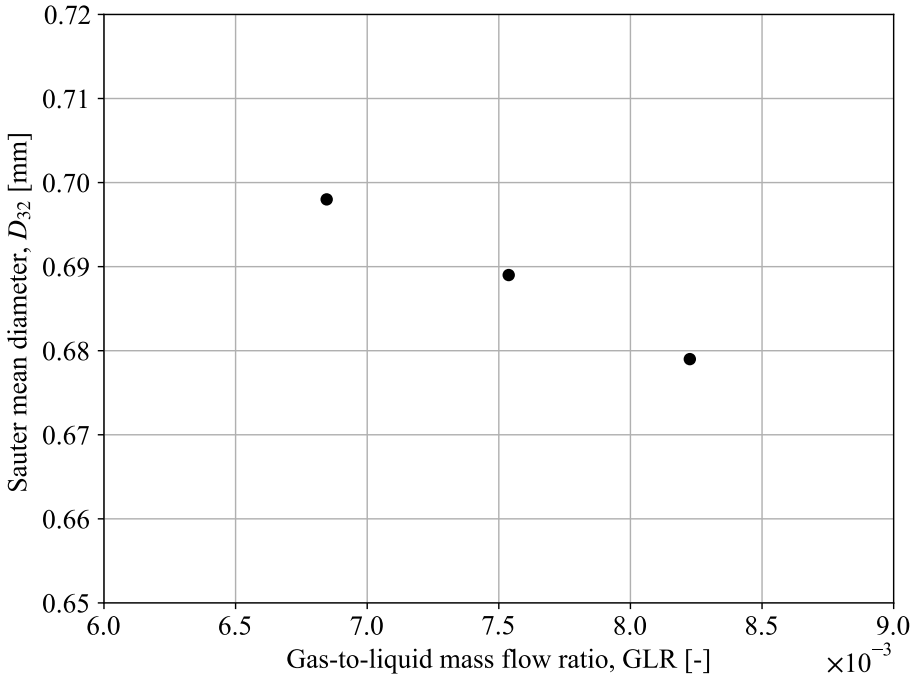

Figure 6.1: The Sauter mean diameter of the droplets is plotted as a function of the gas-to-liquid mass flow ratio, GLR $= \dot{m}_g/\dot{m}_l$.

The decrease in SMD may be explained by two effects. The increase in the airflow rate leads to a larger area occupied by the air in the nozzle orifice. This reduces the available flow area for the liquid which in turn accelerates it. Secondly, the increase in airflow rate increases the velocity of the air which means it exerts a larger shear stress on the liquid to produce a finer atomization spray.

As previously mentioned in Chapter 3 on page 11, instabilities caused by shear stress develop into waves on the surface of the liquid film and eventually break off from the liquid core and form droplets. In this process, kinetic energy is transferred to the liquid through the shear stress. Higher turbulence intensity, I, in the gas phase therefore means more energy is available to break up the liquid (Kourmatzis and Masri 2015).

The turbulence intensity at $x/D = 0$ is presented as contour plots for the different investigated GLRs in Figure 6.2. The black line marks the isosurface of the time-averaged water volume fraction, which has a value of 0.5. The water surrounds the isosurface as a film layer while the air is contained within. It is evident that increasing the GLR results in increased turbulence

intensity in the gas phase region due to the higher velocity. The turbulence intensity remains fairly constant at the isosurface throughout the different simulations which can be attributed to how the data is presented. The time-averaged volume fraction shows the mean location of the isosurface, however, the instantaneous isosurface is constantly changing and experiences the highly turbulent region as well.

The relationship between turbulence intensity and shear stress can therefore explain the observed trend of decreasing SMD with increasing GLR. As the GLR increases, the turbulence intensity in the nozzle also increases, leading to greater shear forces and more efficient breakup of liquid droplets.

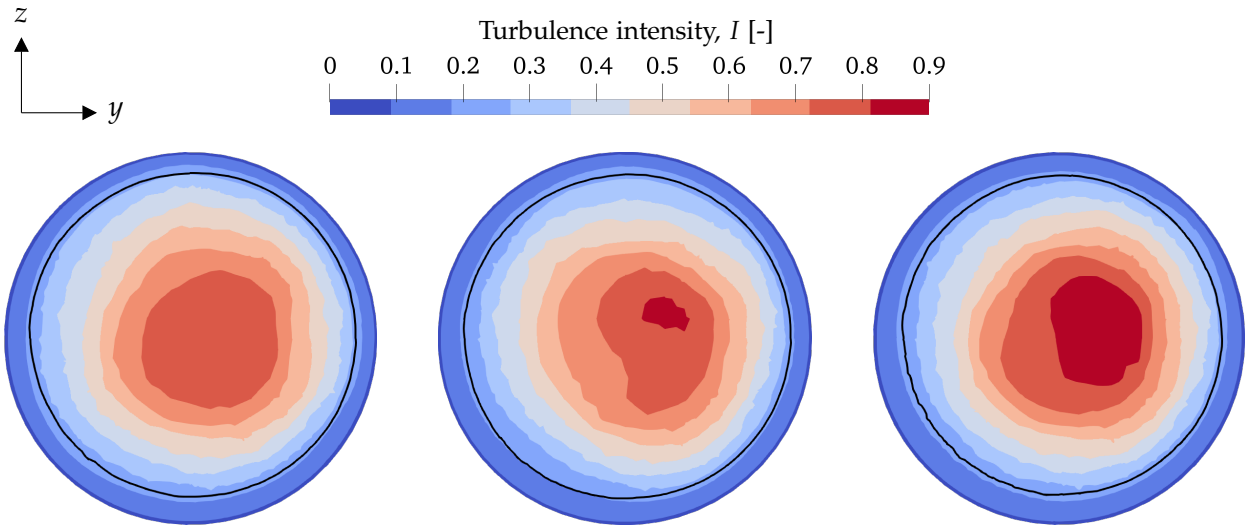

(a) GLR baseline. **(b)** GLR +10 %. **(c)** GLR +20 %.

Figure 6.2: The figures show the contour plot of the turbulent intensity, I, at the investigated gas-to-liquid ratios. The black line represents the isosurface of the time-averaged water volume fraction of 0.5.

6.2 Analysis of Spray Symmetry

In atomization, the spray symmetry and homogeneity are important from a practical perspective to ensure uniform distribution of droplets in the spray. It will therefore be investigated in this section with the validation case. The baseline case is the validation case with a GLR of $6.85{\cdot}10^{-3}$. The symmetry is investigated by examining the time-averaged volume fraction contour downstream of the nozzle orifice. The exact locations are seen in Figure 6.3.

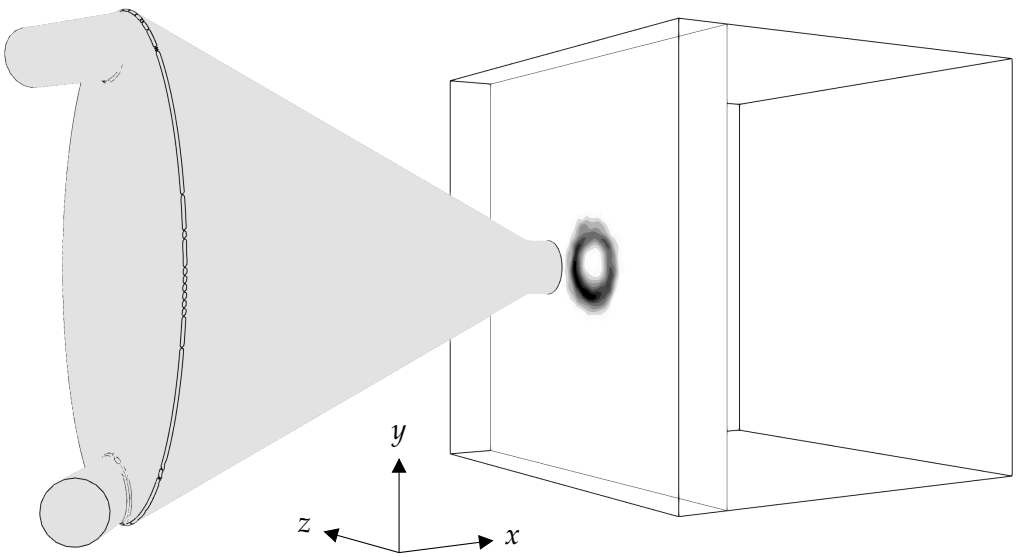

Figure 6.3: Visualisation of the location at which the contour data has been extracted for the symmetry analysis. The first location is inside of the nozzle orifice at $x/D = 0$ and the second location is the plane at $x/D = 1$.

In Figure 6.4, the asymmetric behavior of the spray is evident by the non-uniformity of the time-averaged volume fraction of water. The volume fraction is low due to it being a time-averaged volume fraction of the droplets and ligaments that exit the nozzle. However, it still presents a quantitative view of the asymmetric spray formation, as the time-averaged measurements smooth out transient fluctuations and provide information about the dominant flow patterns. The contour is skewed to the bottom right side which matches the approximate location of the water inlet pipe, which is visible in Figure 6.3. In this area, the water volume fraction is approximately 50% higher compared to the opposite region in the top left part of the contour. This indicates that the water droplets are not evenly distributed due to the arrangement of the inlet channels inside the nozzle.

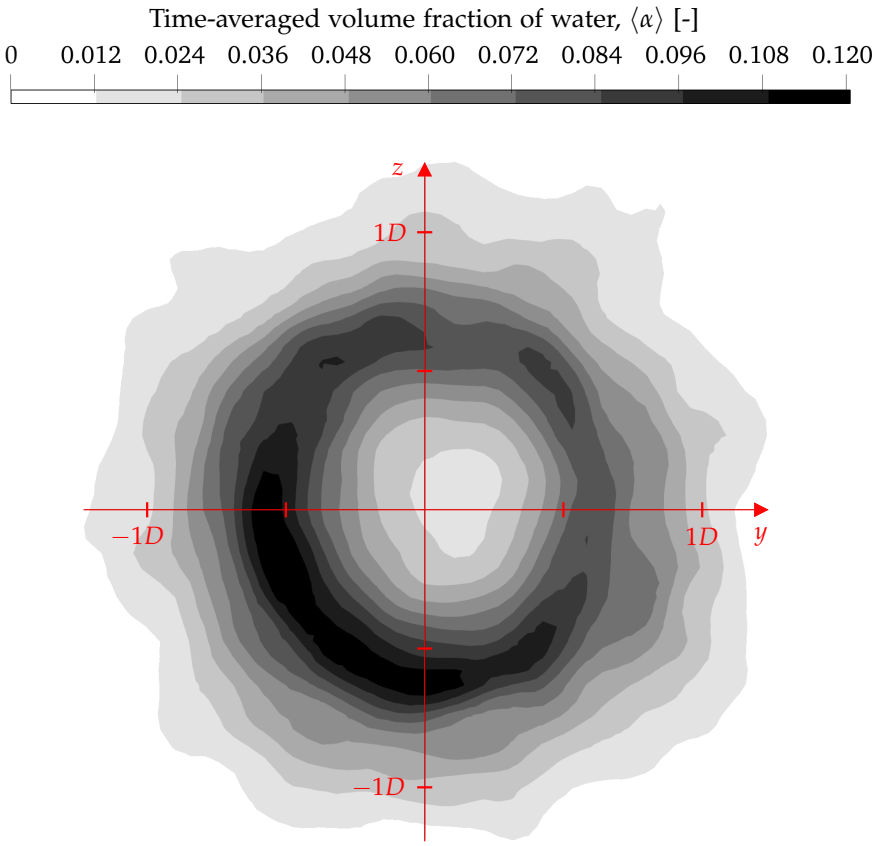

Figure 6.4: Contour plot of the time-averaged water volume fraction at $x/D = 1$.

Furthermore, the time-averaged volume fraction of water is investigated at $x/D = 0$, which is presented in Figure 6.5. Higher volume fractions are visible in the left side of the orifice, since the air takes up more space in the right side of the figure and pushes the water toward the left. This indicates that the water film layer is thickest in the left side and could explain the tendency for water droplets to appear in this region, as shown in Figure 6.4

It can be concluded that the current design of the internal mixing twin-fluid swirl nozzle does not provide a symmetric spray cone. The spray pattern seems to be dependent on the inlet pipes at the investigated GLR. Therefore, the effect of the inclination angle of the inlet pipes will be investigated in the following section.

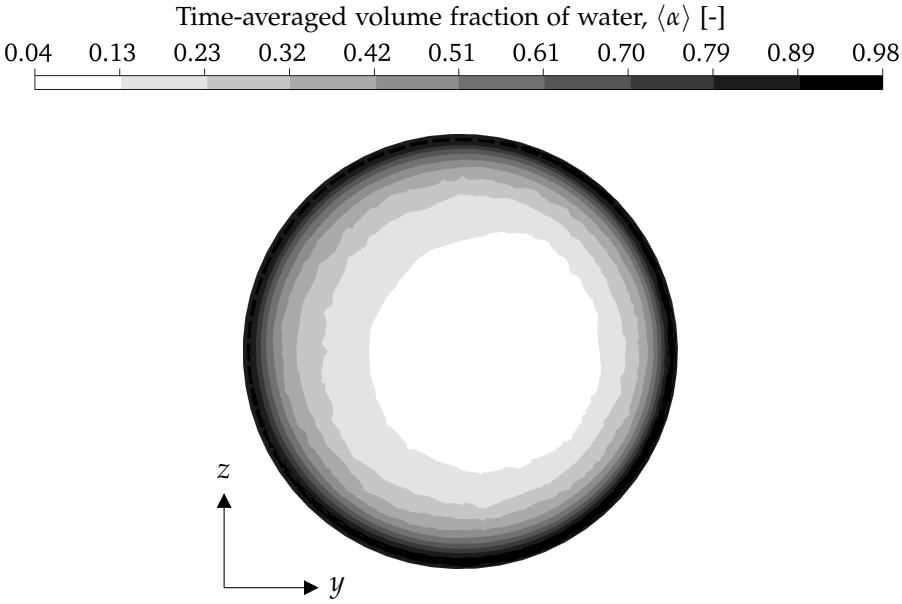

Figure 6.5: Contour plot of the time-averaged water volume fraction at $x/D = 0$.

6.3 Varying Inclination Angle of the Inlet Pipes

The inclination angle of the inlet pipes is an important geometric parameter to investigate as it greatly affects the internal swirling motion and mixing capabilities. Furthermore, it is often preferable to alter the geometric configuration of a component rather than the operational parameters such as the GLR, which would result in increased energy requirements. This section investigates three different inclination angles of 0 °, 27.5 °, and 55 ° presented in Figure 6.6.

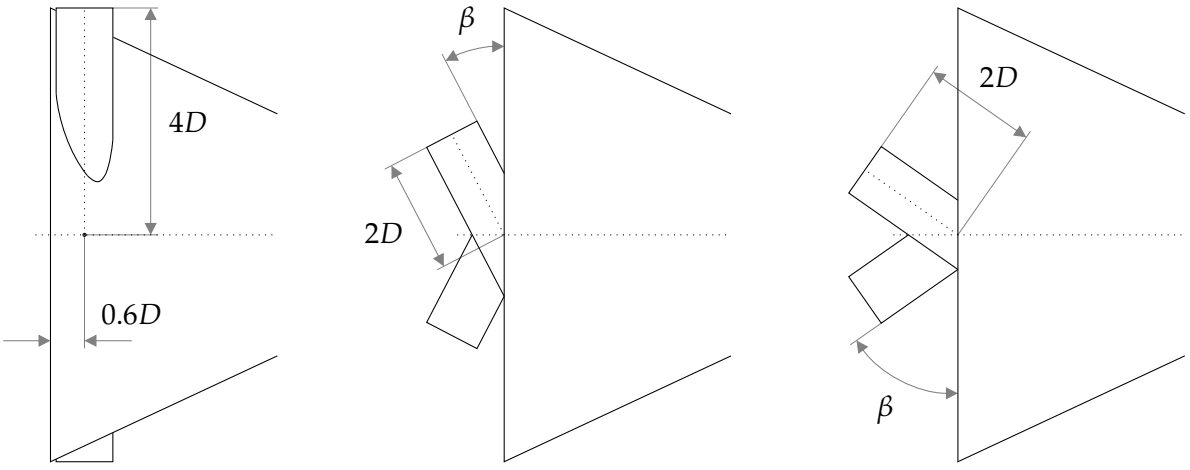

(c) $\beta = 0$ ° **(a)** $\beta = 27.5$ ° **(b)** $\beta = 55$ °

Figure 6.6: Schematic showing the different investigated inclination angles.

The effect of varying the inclination angle of the inlet pipes on the droplet size is visualised in Figure 6.7, where the SMD is plotted as a function of inclination angle, β. The simulations showed that the SMD decreased by 11.9 % with an inclination angle of 0 ° compared to the baseline case of 27.5 °. When the inclination angle increased to 55 °, the SMD increased by approximately 8.3 %. The result may be attributed to the increased turbulent mixing inside the nozzle at an inclination angle of 0 °, which enhances the atomization process.

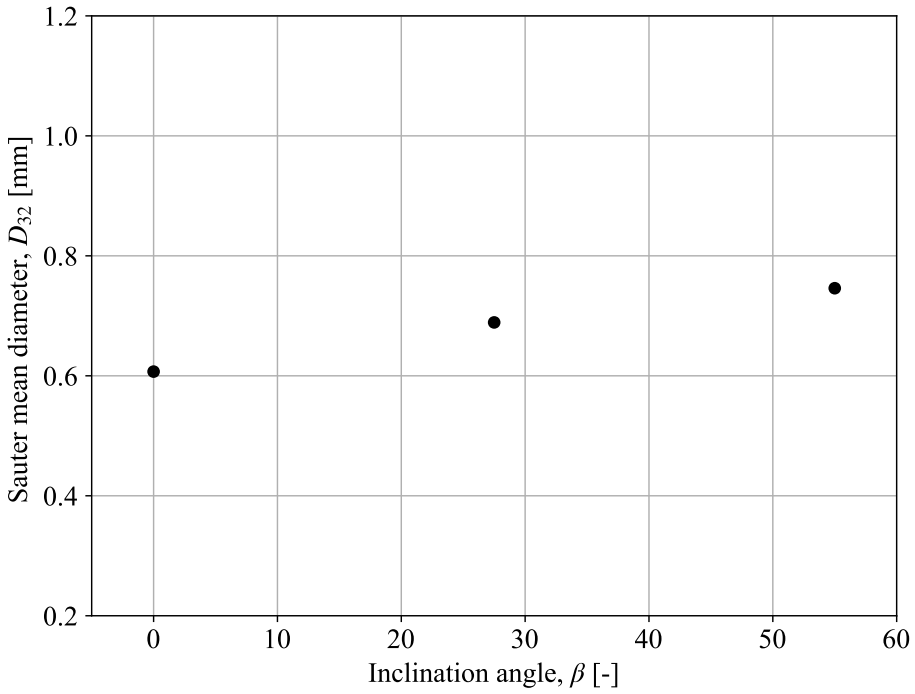

Figure 6.7: The Sauter mean diameter is plotted as a function of the inlet pipe inclination angle, β.

The turbulence intensity is investigated at the nozzle throat at $x/D = 0$, and the result is shown in Figure 6.8. The inclination angle of 0 ° shows a slightly higher turbulence intensity in general, compared to the two other investigated inclination angles. However, the turbulence intensity alone may not fully explain why the SMD decreases at an inclination angle of 0 ° and increases at higher angles. An explanation is that the primary source of turbulence at the nozzle orifice is the shear force between the gas and liquid, and the increased flow velocity. Therefore, the turbulence factors at $x/D = 0$ might not be significantly influenced by changes in the inclination angles.

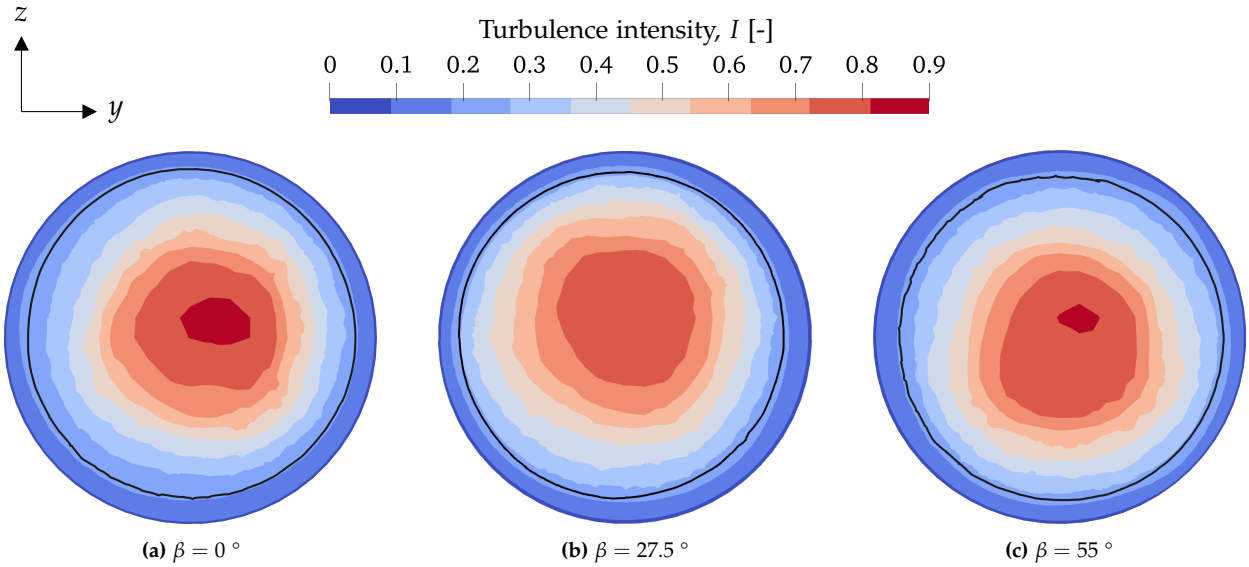

(a) $\beta = 0$ ° **(b)** $\beta = 27.5$ ° **(c)** $\beta = 55$ °

Figure 6.8: The figures show the contour plot of the turbulent intensity, I, at the investigated inlet pipe inclination angles at at $x/D = 0$. The black line represents the isosurface of the time-averaged water volume fraction of 0.5.

As previously mentioned, spray uniformity is an important parameter that seems to depend on the inlet pipes. Therefore, the spray uniformity is investigated for each of the inclination angles. The results are shown in Figure 6.9, where the time-averaged volume fraction of water is visualised at a distance of $x/D = 1$ downstream of the nozzle. It is evident that the least symmetrical spray is produced in Figure 6.9b with an inclination angle of 27.5 °, while both inclination angles of 0 ° and 55 ° produce slightly more symmetric sprays. Furthermore, the region with the highest α values is seen to shift in Figure 6.9c compared to 6.9a and 6.9b, due to the steeper inclination angle.

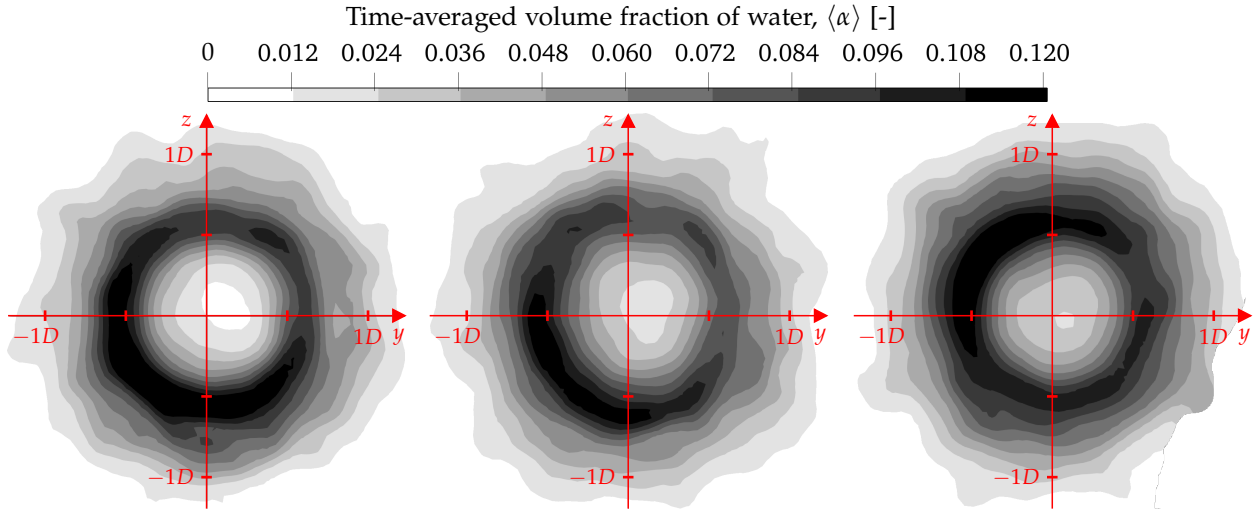

(a) $\beta = 0$ ° **(b)** $\beta = 27.5$ ° **(c)** $\beta = 55$ °

Figure 6.9: The figures show the contour plot of the time-averaged volume fraction of water at the investigated inclination angles at a distance of $x/D = 1$.

The time-averaged volume fraction of water is investigated at $x/D = 0$, which is presented in Figure 6.10. Higher volume fractions dominate in the left part of the orifice at inclination angles of 0 ° and 27.5 °, which also explains why the same region has a higher volume fraction in Figure 6.9. At an inclination angle of 55 ° in Figure 6.10c, the water film layer is thickest in the top part of the orifice as more liquid is directed to that side which affects the spray symmetry. In conclusion, both inclination angles of 0 ° and 55 ° show a slight improvement in spray uniformity. The most optimal design is determined to be an inclination angle of 0 ° due to the spray uniformity and the smallest SMD.

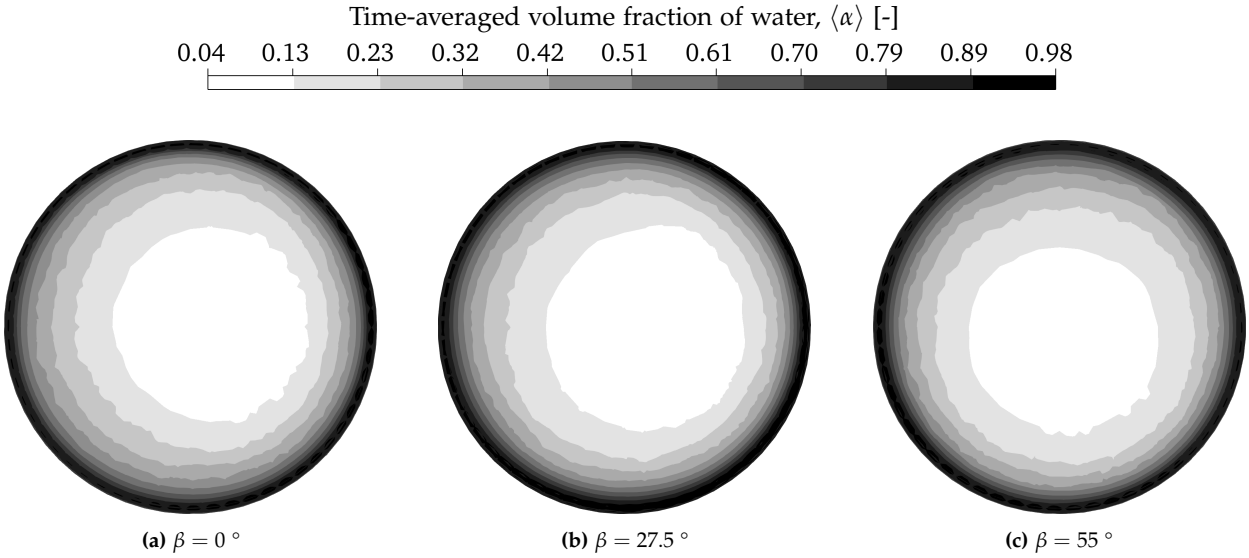

(a) $\beta = 0$ ° **(b)** $\beta = 27.5$ ° **(c)** $\beta = 55$ °

Figure 6.10: The figures show the contour plot of the time-averaged volume fraction of water for the investigated inclination angles at a distance of $x/D = 0$.

7 Conclusion

This work presents a numerical investigation of an internal mixing twin-fluid swirl nozzle. The aim was to understand the atomization performance of the nozzle and its sensitivity to variations in the gas-to-liquid mass flow ratio (GLR) and inclination angle of the inlet pipes, as well as to assess spray symmetry characteristics.

The validation of the CFD model against experimental data yielded promising results with the simulated Sauter Mean Diameter (SMD) deviating by 16.9 % from the experimental values. This validation provided confidence in the accuracy and reliability of the CFD model for simulating the atomization process in the investigated swirl nozzle.

Furthermore, the effect of varying the GLR on the atomization performance was investigated and revealed 20 % increase in GLR resulted in a 2.8 % decrease in SMD. This observation is consistent with the findings in the literature. The spray symmetry was investigated using the contour of the time-averaged water volume fraction downstream of the nozzle orifice at a distance corresponding to one orifice diameter, $x/D = 1$. The analysis revealed that the water droplets predominantly left the nozzle orifice in the same side as the inlet water pipe. This asymmetry in the distribution of droplets suggests potential challenges in achieving uniform spray coverage.

In this study, three inclination angles of 0 °, 27.5 °, and 55 ° have been investigated. The SMD decreased by 11.9 % with an inclination angle of 0 ° compared to the baseline case of 27.5 °. When the inclination angle increased to 55 °, the SMD increased by approximately 8.3 %. The result might be attributed to the increased turbulent mixing inside the nozzle with an inclination angle of 0 °, which would enhance the atomization process. Furthermore, the spray symmetry was investigated for each of the inclination angles. The least symmetrical spray was achieved with an inclination angle of 27.5 °, while an angle of 0 ° and 55 ° produced slightly more symmetric sprays. Furthermore, the region with the highest α values was seen to shift for an inclination angle of 55 °. Based on the findings in this study, the most optimal design was determined to be an inclination angle of 0 ° due to the improved spray symmetry and lowest SMD.

8 Suggestions for Further Work and Discussion

In this study, CFD simulations were conducted to investigate the atomization performance of a twin-fluid internal mixing swirl nozzle. While the simulations provided valuable insights into the spray characteristics and flow dynamics, several limitations were encountered that could impact the accuracy and reliability of the results.

One limitation of the CFD simulations was the use of incompressible fluid models for both the water and gas phases. While incompressible flow assumptions are commonly employed in many CFD simulations, they may not fully capture the compressibility effects that could be present, especially at high flow velocities or in regions with significant pressure gradients. To improve the accuracy of the results, compressible fluid models should be considered due to the high-velocity flow regions near the nozzle exit.

Another limitation was the necessity to incorporate fillets into the nozzle geometry due to poor mesh quality around sharp corners. This alteration could potentially impact the flow characteristics, spray formation, and atomization performance compared to the original experimental conditions. To address this limitation and improve the accuracy of the simulations, efforts should be made to refine the mesh around sharp corners and complex geometrical features to better capture flow characteristics and minimise numerical errors. However, due to the turbulent structure of the flow field inside the nozzle, this limitation was not deemed too influential.

Additionally, consideration could be given to employing advanced meshing techniques, such as adaptive mesh refinement to enhance mesh quality and resolution in critical regions of the flow domain. This could also improve the computational cost of the simulations.

An important aspect that requires further investigation is the droplet separation and coalescence. Understanding droplet separation mechanisms is important for accurately predicting the size distribution and dispersion of droplets in the spray. Droplet coalescence is the process where smaller droplets collide and merge to form larger droplets. This phenomenon affects the overall droplet size distribution and can lead to non-uniform spray patterns.

The simulations in this study were carried out with constant inlet velocity profiles without

induced eddies. No turbulent structures were therefore present in both inlet pipes which could potentially affect the results. However, due to the turbulent mixing inside the nozzle, this was not accounted for. In future studies, this would be interesting to investigate to see whether it has any significant influence on the results. This could be done by providing a boundary condition that fluctuates in time and produces synthetic eddies. A second approach would be to cycle the inlet pipe flow a finite number of times back to the inlet, for the turbulent structures to form naturally due to shear stress.

Bibliography

Ochowiak, Marek (2016). "The experimental studies on atomization for conical twin-fluid atomizers with the swirl motion phenomenon". In: *Chemical Engineering and Processing - Process Intensification* 109, pp. 32–38. ISSN: 0255-2701. DOI: https://doi.org/10.1016/j.cep.2016.08.010.

Tian, Yankang (2019). "Integrated CFD Modelling for Nozzle Design for Fog Generation". PhD thesis. University of Strathclyde.

Ashgriz, Nasser (Jan. 2011). *Handbook of Atomization and Sprays: Theory and Applications*. Springer Science+Business Media, LLC, p. 935. ISBN: 978-1-4419-7263-7. DOI: 10.1007/978-1-4419-7264-4.

Nazeer, Yasir et al. (Oct. 2020). "Atomization Mechanism of Internally Mixing Twin-Fluid Y-Jet Atomizer". In: *Journal of Energy Engineering* 147. DOI: 10.1061/(ASCE)EY.1943-7897.0000723.

Zhou, Yuegui et al. (2010). "Experimental investigation and model improvement on the atomization performance of single-hole Y-jet nozzle with high liquid flow rate". In: *Powder Technology* 199.3, pp. 248–255. ISSN: 0032-5910. DOI: https://doi.org/10.1016/j.powtec.2010.01.013.

Watanawanyoo, Pipatpong et al. (2011). "Experimental investigations on spray characteristics in twin-fluid atomizer". In: vol. 24, pp. 816–822. DOI: 10.1016/j.proeng.2011.11.2743.

Lee, Sang Ji, Ji Yeop Kim, and Jung Goo Hong (Apr. 2023). "Asymmetric Spray Characteristics According to Y-Jet Nozzle Orifice Shape and Spray Conditions". In: *ACS Omega* 8 (16), pp. 14490–14498. ISSN: 24701343. DOI: 10.1021/acsomega.3c00016.

Barbieri, Matheus Rover, Lydia Achelis, and Udo Fritsching (Nov. 2023). "Effect of Y-jet nozzle geometry and operating conditions on spray characteristics and atomizer efficiency". In: *International Journal of Multiphase Flow* 168. ISSN: 03019322. DOI: 10.1016/j.ijmultiphaseflow.2023.104585.

Ludwig, Wojciech et al. (Feb. 2022). "CFD modelling of a powder spraying nozzle used for dry coating". In: *Chemical Engineering Research and Design* 178, pp. 550–566. ISSN: 02638762. DOI: 10.1016/j.cherd.2022.01.001.

Liu, He et al. (Dec. 2022). "Atomization Characteristics of Special-Design Pneumatic Two-Fluid Nozzles for Helicopter Main Reducers: A Numerical and Experimental Investigation". In: *Aerospace* 9 (12). ISSN: 22264310. DOI: 10.3390/aerospace9120834.

Mohammadi, Alireza, Fathollah Ommi, and Zoheir Saboohi (2022). "Experimental and numerical study of a twin-fluid two-phase internal-mixing atomizer". In: *Journal of Thermal Analysis and Calorimetry* 147.5, pp. 3673–3687.

Han, Han et al. (2020). "Effect of water supply pressure on atomization characteristics and dust-reduction efficiency of internal mixing air atomizing nozzle". In: *Advanced Powder Technology* 31.1, pp. 252–268. ISSN: 0921-8831. DOI: https://doi.org/10.1016/j.apt.2019.10.017.

Trautner, Elias et al. (2023). "Primary atomization of liquid jets: Identification and investigation of droplets at the instant of their formation using direct numerical simulation". In: *International Journal of Multiphase Flow* 160, p. 104360. ISSN: 0301-9322. DOI: https://doi.org/10.1016/j.ijmultiphaseflow.2022.104360.

Zhang, Feichi et al. (Jan. 2023). "Numerical simulations of air-assisted primary atomization at different air-to-liquid injection angles". In: *International Journal of Multiphase Flow* 158. ISSN: 03019322. DOI: 10.1016/j.ijmultiphaseflow.2022.104304.

Hua, Jinsong et al. (Feb. 2024). "A numerical modeling framework for predicting the effects of operational parameters on particle size distribution in the gas atomization process for Nickel-Silicon alloys". In: *Powder Technology* 435. ISSN: 1873328X. DOI: 10.1016/j.powtec.2024.119408.

Chen, Bo et al. (2022). "DPM-LES investigation on flow field dynamic and acoustic characteristics of a twin-fluid nozzle by multi-field coupling method". In: *International Journal of Heat and Mass Transfer* 192, p. 122927. ISSN: 0017-9310. DOI: https://doi.org/10.1016/j.ijheatmasstransfer.2022.122927.

Basha, Nausheen, Ahmed Kovacevic, and Sham Rane (2019). "Analysis of Oil-Injected Twin-Screw Compressor with Multiphase Flow Models". In: *Designs* 3.4. ISSN: 2411-9660. DOI: 10.3390/designs3040054.

Lain, S. and M. Sommerfeld (2003). "Turbulence modulation in dispersed two-phase flow laden with solids from a Lagrangian perspective". In: *International Journal of Heat and Fluid Flow* 24 (4), pp. 616–625. ISSN: 0142727X. DOI: 10.1016/S0142-727X(03)00055-9.

Rodi, Wolfgang (Feb. 2006). "DNS and LES of some engineering flows". In: *Fluid Dynamics Research* 38 (2-3), pp. 145–173. ISSN: 01695983. DOI: 10.1016/j.fluiddyn.2004.11.003.

Basse, Nils T. (2017). "Turbulence Intensity and the Friction Factor for Smooth- and Rough-Wall Pipe Flow". In: *Fluids* 2.2. ISSN: 2311-5521. DOI: 10.3390/fluids2020030.

Zaremba, Matouš et al. (2017). "Low-pressure twin-fluid atomization: Effect of mixing process on spray formation". In: *International Journal of Multiphase Flow* 89, pp. 277–289. ISSN: 0301-9322. DOI: https://doi.org/10.1016/j.ijmultiphaseflow.2016.10.015.

Watanawanyoo, Pipatpong et al. (Jan. 2012). "Experimental Study on the Spray Characteristics of an Air Assisted Atomizer with Internal Mixing Chamber". In: *European Journal of Scientific Research* 84, pp. 507–521.

Ashgriz, N (1990). *Coalescence and separation in binary collisions of liquid drops*.

Qian, By J (1997). *Regimes of coalescence and separation in droplet collision*.

Shrestha, Kendra et al. (May 2023). "Primary spray breakup from a nasal spray atomizer using volume of fluid to discrete phase model". In: *Physics of Fluids* 35.5, p. 053312. ISSN: 1070-6631. DOI: 10.1063/5.0150890.

Versteeg, H. and W. Malalasekera (2007). *An Introduction to Computational Fluid Dynamics e-book: The Finite Volume Method*. Pearson Education. ISBN: 9781405891042. URL: https://books.google.dk/books?id=dlC8MgEACAAJ.

Brackbill, J.U, D.B Kothe, and C Zemach (1992). "A continuum method for modeling surface tension". In: *Journal of Computational Physics* 100.2, pp. 335–354. ISSN: 0021-9991. DOI: https://doi.org/10.1016/0021-9991(92)90240-Y.

Franck, Nicoud and Frédéric Ducros (Sept. 1999). "Subgrid-Scale Stress Modelling Based on the Square of the Velocity Gradient Tensor". In: *Flow Turbulence and Combustion* 62, pp. 183–200. DOI: 10.1023/A:1009995426001.

McGinn, Paul, Cyril Crua, and Konstantina Vogiatzaki (Dec. 2018). "Assessing the role of surface tension force to the simulation of sub-grid scale interaction of turbulence and cavitation under realistic diesel injection conditions". In.

Hirt, C.W and B.D Nichols (1981). "Volume of fluid (VOF) method for the dynamics of free boundaries". In: *Journal of Computational Physics* 39.1, pp. 201–225. ISSN: 0021-9991. DOI: https://doi.org/10.1016/0021-9991(81)90145-5.

Gamet, Lionel et al. (2020). "Validation of volume-of-fluid OpenFOAM® isoAdvector solvers using single bubble benchmarks". In: *Computers Fluids* 213, p. 104722. ISSN: 0045-7930. DOI: https://doi.org/10.1016/j.compfluid.2020.104722.

Karch, Grzegorz K. et al. (2013). "Visualization of piecewise linear interface calculation". In: *2013 IEEE Pacific Visualization Symposium (PacificVis)*, pp. 121–128. DOI: 10.1109/PacificVis.2013.6596136.

Panão, M. R. O. (2023). "Why drop size distributions in sprays fit the lognormal". In: *Physics of Fluids* 35.1, p. 011701. ISSN: 1070-6631. DOI: 10.1063/5.0135510. URL: https://doi.org/10.1063/5.0135510.

Kissell, Robert and Jim Poserina (2017). "Chapter 4 - Advanced Math and Statistics". In: *Optimal Sports Math, Statistics, and Fantasy*. Ed. by Robert Kissell and Jim Poserina. Academic Press, pp. 103–135. ISBN: 978-0-12-805163-4. DOI: https://doi.org/10.1016/B978-0-12-805163-4.00004-9.

Bernardes, Patrícia et al. (Oct. 2010). "Assessment of hydrophobicity and roughness of stainless steel adhered by an isolate of Bacillus cereus from a dairy plant". In: *Brazilian journal of microbiology : [publication of the Brazilian Society for Microbiology]* 41, pp. 984–92. DOI: 10.1590/S1517-838220100004000017.

Štigler, Jaroslav (June 2012). "Analytical Velocity Profile in Tube for Laminar and Turbulent Flow". In: DOI: 10.13140/2.1.3153.5046.

Roache, Patrick J. (1994). "Perspective: A Method for Uniform Reporting of Grid Refinement Studies". In: *Journal of Fluids Engineering* Vol. 116 of 405.

ANSYS, Inc. (Jan. 29, 2009). *ANSYS FLUENT User's Guide*, version 12.0.

Ochowiak, Marek, Lubomira Broniarz-Press, and Szymon Woziwodzki (2014). "Reverse-Lens Technique in Process Visualization". In: *Chemical Engineering & Technology* 37.3, pp. 505–510. DOI: https://doi.org/10.1002/ceat.201200142.

Kourmatzis, Agisilaos and A.R. Masri (Feb. 2015). "Air assisted atomization of liquid jets in varying levels of turbulence". In: *Journal of Fluid Mechanics* 764, pp. 95–132. DOI: 10.1017/jfm.2014.700.

A Numerical Determination of Droplet Size

A function object called *RegionSizeDistribution* in OpenFOAM is used to determine the droplet size from the interface between the gas and liquid phases. It uses the volume fraction to split the domain into regions of separate phases based on a threshold value set to 0.5. The function object is applied on the outlet boundary patch and measures the size and number of droplets traversing the boundary as a function of time. It handles non-spherical droplets by converting the volumes into equivalent spheres and measures the resulting diameter which is visualised in Figure 4.3. The implementation in the OpenFOAM controlDict file is seen in the code snippet below. The maximum diameter of the droplets is set to 0.004 m as this was far beyond the largest droplet observed in the experimental data from Ochowiak (2016). It is set to measure the droplets on the box outlet patch and write the data every time the simulation writes a time step.

```
regionSizeDistribution
{
    type            regionSizeDistribution;
    libs            ("libfieldFunctionObjects.so");
    executeControl  writeTime;
    writeControl    writeTime;
    alpha           alpha.water;
    patches         (box_outlet);
    threshold       0.5;
    fields          (p U);
    nBins           100;
    maxDiameter     0.004;
    minDiameter     0;
    setFormat       csv;
}
```

B Downstream Distance

To validate the numerical model, the results are compared to the experimental data from Ochowiak (2016). However, two important details have not been stated by the author, which may result in inaccurate CFD predictions. Firstly, the location at which the droplet size distribution was measured during the experiments has not been specified. Secondly, the duration between the start of the experiments and the time at which the droplet size measurements were captured was not provided either.
Therefore, a study is conducted to simulate the droplet size distribution at different distances from the nozzle exit using a medium-sized mesh with a cell size of 0.165 mm in the refinement regions. The simulations are run for approximately 0.42 seconds and the droplets are measured from 0.32 s to 0.42 s.

Figures B.1a and B.1b show the PDF and histogram of the droplet size distribution at a downstream distance of $x/D = 8$ and $x/D = 15$ respectively. It is evident that there is some discrepancy between the numerical CFD prediction and the experimental measurements, and it is difficult to tell which is the most accurate. The CFD model generally overpredicts the droplet size at a diameter of approximately 0.5 mm while it underpredicts at diameters of 0.7 - 1 mm. However, there is a larger overlap between the experimental and CFD PDF in Figure B.1a compared to Figure B.1b.

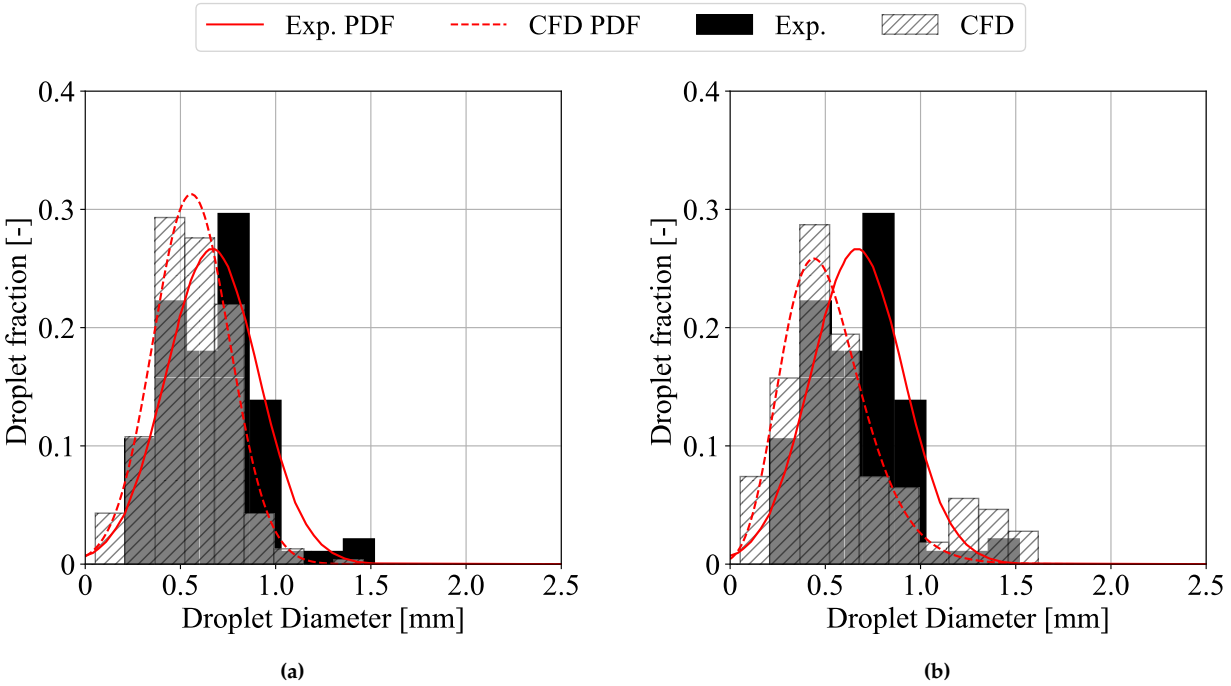

Figure B.1: Comparison of experimental and simulated droplet measurements at $x/D = 8$ and $x/D = 15$ downstream of the nozzle respectively.

The mean droplet diameter measured in both the experimental data and the CFD simulations is presented in Table B.1. It is evident that the downstream distance of $x/D = 15$ is more accurate on this specific parameter. However, it is due to the overprediction of large droplets which contribute to the larger mean diameter. The result of the CFD simulation at $x/D = 8$ is a more valid representation of the experimental data, as it captures the droplet size distribution more accurately.

Table B.1: Comparison of mean diameter in the CFD simulation

	Mean diameter [mm]
CFD at $x/D = 8$	0.56
CFD at $x/D = 15$	0.62
Exp.	0.66

Based on the comparison of the droplet size distribution with the medium-sized mesh, the downstream distance of $x/D = 8$ provides the best representation of the experimental droplet size distribution. Therefore, the droplet size distribution will be measured at this distance.

C Coarse and Medium Mesh Statistics

Coarse Mesh

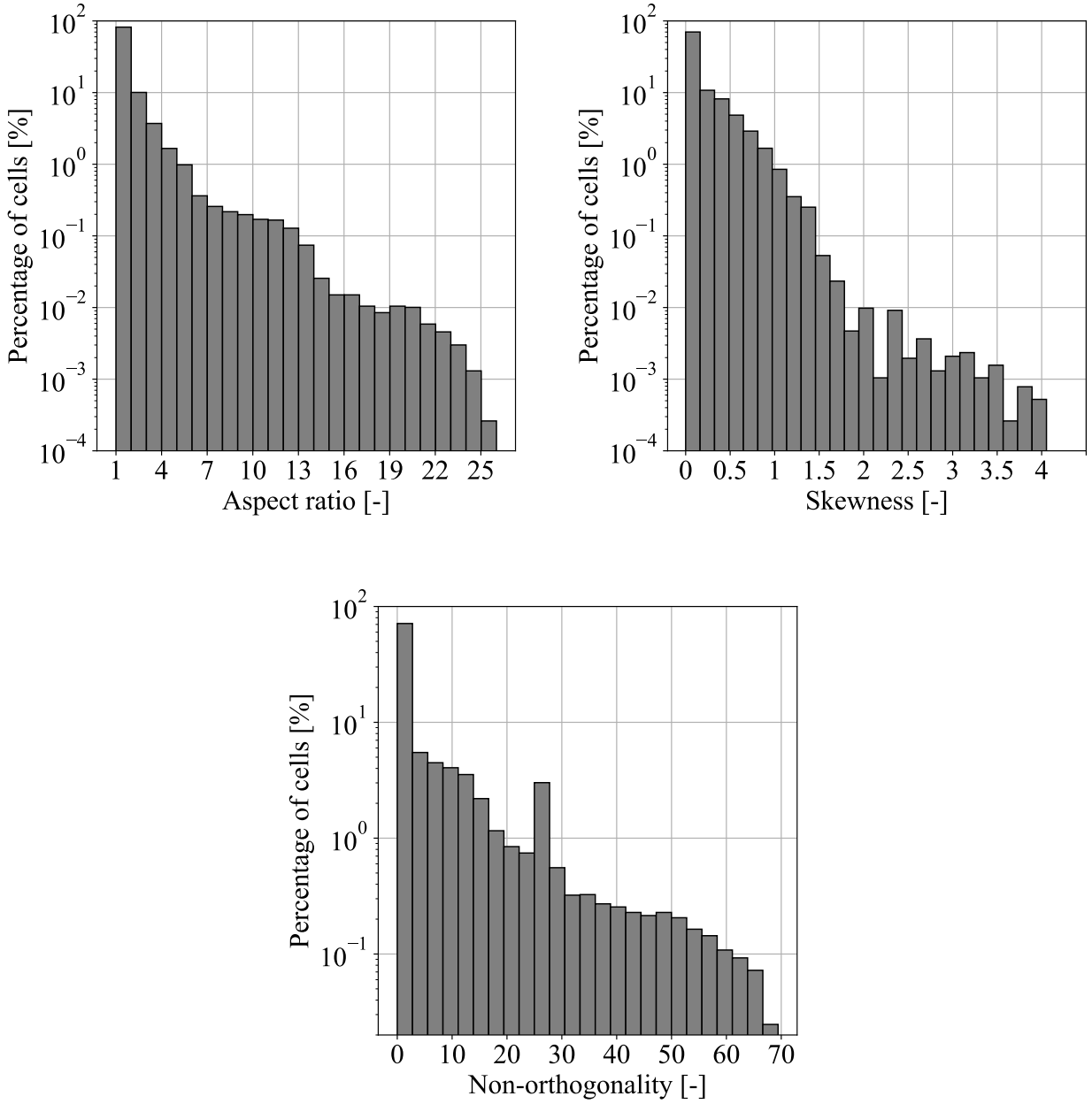

Figure C.1: The figures show the percentage of cells in the coarse mesh with a given cell aspect ratio, skewness, and non-orthogonality.

Medium Mesh

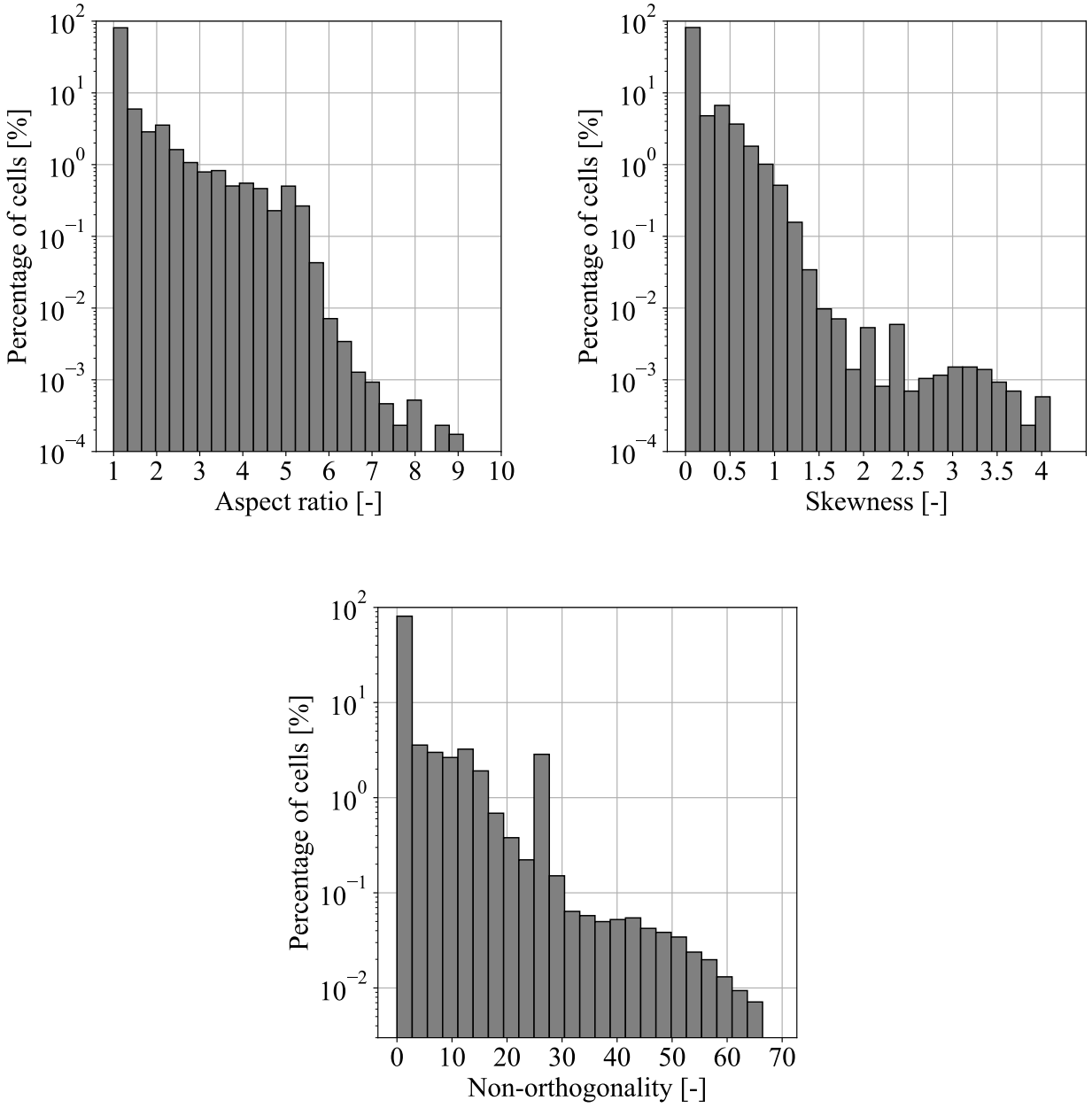

Figure C.2: The figures show the percentage of cells in the medium mesh with a given cell aspect ratio, skewness, and non-orthogonality.